EFFECTS OF RESONANT VIBRATIONS ON DROPLET MOBILITY AND

DROPWISE CONDENSATION

A Thesis

by

CHIRAG ANAND DESHPANDE

Submitted to the Graduate and Professional School of
Texas A&M University
in partial fulfillment of the requirements for the degree of

MASTER OF SCIENCE

Chair of Committee,	Jorge L. Alvarado
Committee Members,	M. Cynthia Hipwell
	Mark Kimber
Head of Department,	Guillermo Aguilar

December 2021

Major Subject: Mechanical Engineering

ABSTRACT

In recent years, enhancements in dropwise condensation have been achieved by formulating, fabricating, and using hydrophobic coatings with all sorts of surface features. Reduction in contact angle hysteresis and better droplet sliding properties have been achieved by incorporating nanoscale features on surfaces. However, most recently developed coatings still face considerable implementation challenges due to their lack of long-term durability and affordability. Therefore, methods that rely on external stimuli for faster droplet shedding during dropwise should be explored. Recently, the use of vibrations to promote droplet shedding in DWC has been studied. However, it is important to identify the corresponding resonance frequencies to keep vibration amplitudes low for optimal system performance.

In the first part of this study, four droplets within 3 - 5 μL and five different vertically oriented surfaces with contact angles ranging from 70º - 110º were used. Experiments were conducted to determine the resonance frequencies for each droplet-surface combination. In the second stage, the surface was imposed with the resonance frequencies and frequencies within ± 8 Hz of the resonance frequencies for the respective droplet volumes. The acceleration of the surface was adjusted until droplet sliding occurred. It was observed that minimum acceleration values required for droplets to slide were at their corresponding resonance frequencies.

In the study, condensation experiments were conducted under constant subcooling conditions for copper and PTFE without vibration and under resonant vibrations. The effects of imposing a single frequency and amplitude as well as frequency sweeps on

condensation rates were explored. It was found that for both surfaces, vibrations led to enhancement in condensation rates with maximum enhancement achieved when high-to-low frequency sweep was imposed.

In summary, vibrations at resonant frequencies have led to efficient drop mobility on the surface and improved dropwise condensation rates. The potential use of resonant vibrations in condensation systems should improve their overall thermal performance considerably.

DEDICATION

I dedicate this thesis to my parents Dr. Anand Deshpande and Dr. Meenakshi Deshpande.
I am grateful for your constant support throughout the course of my master's degree and
my life. I would not have been the person I am, without you. Thank you for everything.

ACKNOWLEDGEMENTS

CONTRIBUTORS AND FUNDING SOURCES

Contributors

I would like to acknowledge my committee chair Dr. Jorge Alvarado and my committee members Dr. Mark Kimber and Dr. Cynthia Hipwell for their invaluable contributions. Furthermore, I would like to acknowledge the contributions from Dr. Stanley Ling and Dr. Chun Wei Yao. I would also like to acknowledge the contributions from former students in the lab, Sarojeet Deb and Zaki Mohsin as well as the contributions of my lab mates Nikhil Singh Pundir, Shitiz Sehgal and Pavanrohith Govindraju.

Funding Sources

Graduate study was funded by limited funds provided by Dr. Alvarado.

NOMENCLATURE

a	RMS value for acceleration
A	RMS value for amplitude
Bo	Bond number
D	Distance from the drop center to any point on the droplet outlines
DWC	Drop wise condensation
f	Frequency
F	Pinning force per unit length
FWC	Film wise condensation
g	Acceleration due to gravity
h_{fg}	Latent heat of water
h_{latent}	Heat transfer coefficient for condensation
I	Vibrational intensity
j	Resonance mode
m	Mass of the droplet
$m_{condensate}$	Mass of condensate
N_s	Nucleation site density
p	Arc length from drop edge to the drop center
q_j	Wave factor for one dimensional capillary wave
$\dot{Q}_{latent}$	Condensation heat transfer rate
Q''_{latent}	Condensation heat flux

$\%RH$	Relative humidity
R	Droplet radius
SA	Surface area for condensation
t	Time
T_b	Bulk moist air temperature
T_s	Surface temperature
T_{sat}	Saturation temperature
U	Potential energy barrier
V	Droplet volume
γ	Surface tension
δ	Stokes length
$\Delta\theta$	Contact angle hysteresis (CAH)
θ_a	Advancing contact angle
θ_e	Static contact angle (SCA)
θ_r	Receding contact angle
μ	Kinematic viscosity
ρ	Density of water
ρ^e	Density of fluid surrounding the droplet
σ_{θ_e}	Standard deviation in static contact angle
ω_c	Capillary frequency
ω_j	Angular resonance frequency for the jth mode

Subscripts:

j	Resonance mode
L	Liquid
V	Vapor
S	Solid

TABLE OF CONTENTS

LIST OF FIGURES

LIST OF TABLES

CHAPTER I

INTRODUCTION

1.1 Condensation

Phase change is one of the most efficient methods of heat transfer due to the large difference in internal energy (latent heat) between the two phases, which is absorbed or released during the process. Condensation is one such process in which a condensable vapor releases its latent heat when the temperature is reduced below its saturation temperature for a given pressure [1]. The vapor temperature normally goes below the saturation temperature upon contact with a cold solid surface. However, condensation can also occur at a free liquid surface or at a gas interface when the temperature of the liquid or gas exposed to the vapor goes below saturation temperature. Gases like air, nitrogen, and carbon dioxide, which cannot be liquified at normal compression pressures are called non-condensable gases (NCGs). Condensation can occur in the presence or in the absence of non-condensable gases. The heat transfer rate in the presence of NCGs is typically less as compared with the rate in absence of NCGs due to the added thermal resistance due to accumulation of NCGs near the condensation surface as shown by Al-Shammari [2]. The condensation heat transfer increases with an increase in mole fraction of the condensable gases [3]. Water Vapor condensation in presence of NCGs like air is more common in industry and ubiquitous in nature, hence it will be one of the foci of this study.

There are two main mechanisms through which condensation occurs, namely film wise condensation (FWC) and drop wise condensation (DWC) as shown in Fig. 1. FWC is more common and occurs with the condensate completely wetting the surface to form a

liquid film which grows in thickness along the flow direction of the film [1]. FWC of water vapor normally occurs on clean, smooth, and hydrophilic surfaces. The film of liquid formed during the initial phase of condensation, keeps increasing in thickness, thus increasing the thermal resistance to further heat transfer. This leads to a reduction in condensation heat transfer rates during FWC. In DWC, condensate drops form at nucleation sites on the surface, grow due to further condensation and through coalescence with neighboring drops, and then the drops shed under the influence of gravity (if the surface is inclined). While moving they coalesce with other drops in the lower regions of the surface, resulting in further droplets sweeping off the surface. This leads to a formation of a fresh area available for further nucleation and thus an increase in condensation rate leading to heat transfer coefficients an order of magnitude greater than those for FWC [4].

(a)   *(b)*
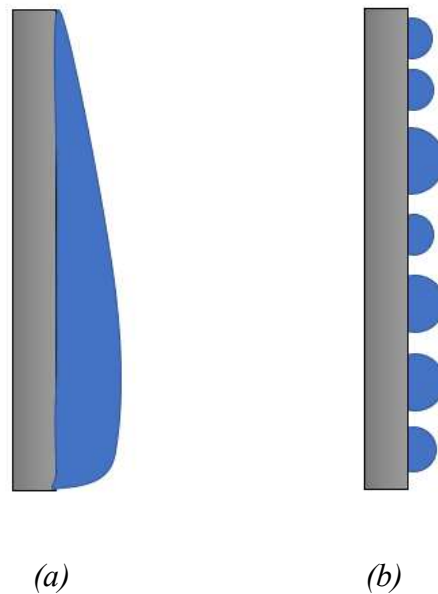
Figure 1. *(a)* Film-wise condensation *(b)* dropwise condensation

DWC mechanism is governed by the Classical Nucleation Theory (CNT) which states that nucleation rates are higher on surfaces having high surface energy (hydrophilic) and high nucleation site density (surface imperfections). However, hydrophilic surfaces tend to transition to FWC since the drops that form tend to spread and coalesce to form a film. Hence, it is preferred to use a slightly hydrophobic surface to have a sustained dropwise condensation mode. Furthermore, the amount of sub-cooling (temperature difference between the condensing vapor and the surface) also affects the transition from DWC to FWC. A higher level of sub-cooling leads to a higher amount of drop formation, growth and coalescence and may lead to film formation as the drops shed along the surface [5].

The heat transfer rate in DWC is primarily affected by the departure drop size and the drop mobility on the surface. A smaller departure drop size leads to a lesser thermal resistance to heat transfer, while high mobility leads to a faster coalescence and shedding rate thus exposing new area for fresh droplets to condense. Therefore, to improve DWC rates it is imperative to study the whole behavior of drops on solid surfaces.

1.2 Drops on solid surfaces

For a drop placed on a horizontal surface as shown in fig. 2, the angle made by the liquid-vapor interface with the solid surface beneath the drop is defined as the static contact angle (SCA) of the drop with the surface. Assuming that the drop and surface are kept in ambient conditions, SCA is dependent on the surface tension of the liquid and the surface energy of the solid as given by Young's equation [6]

$$\gamma_{LV} cos(\theta_e) = \gamma_{SV} - \gamma_{SL} \tag{1}$$

where, γ_{LV}, γ_{SV}, γ_{SL} are the liquid-vapor, solid-vapor, and solid-liquid surface tensions

respectively and θ_e is the static contact angle

(a)   (b)
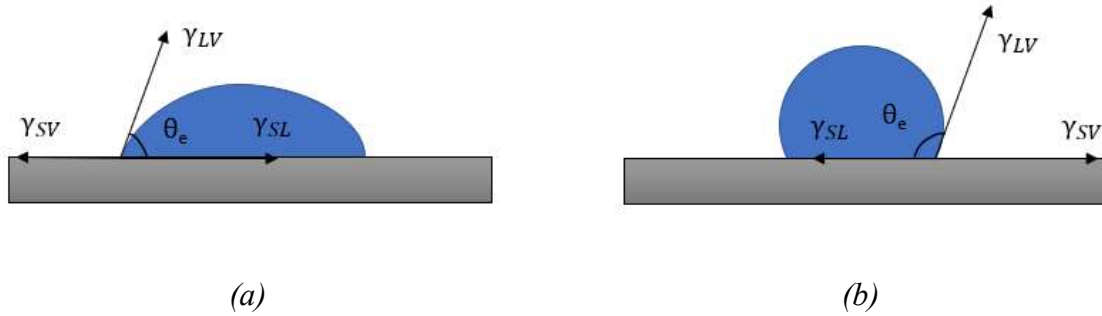
Figure 2. Static contact angle on *(a)* hydrophilic and *(b)* hydrophobic surfaces

The area on the surface which the droplet wets is defined as the contact area, while the circumference is called the contact line or the triple line, since three phases (solid, liquid and gas) co-exist at the line. SCA, which is typically independent of the volume of the droplet, dictates the wetting behavior of the liquid on the surface. For a water droplet on a surface, a SCA of less than 90⁰ indicates that the liquid wets the surface, or that the surface is hydrophilic. A SCA of greater than 90⁰ indicates that the liquid poorly wets the surface, or that the surface is hydrophobic. For drops resting or sliding on inclined surfaces, drops deform in the direction of gravity leading to unequal contact angles at the leading and trailing ends of the drop diameter in the direction of the force as shown in the Fig. 3.
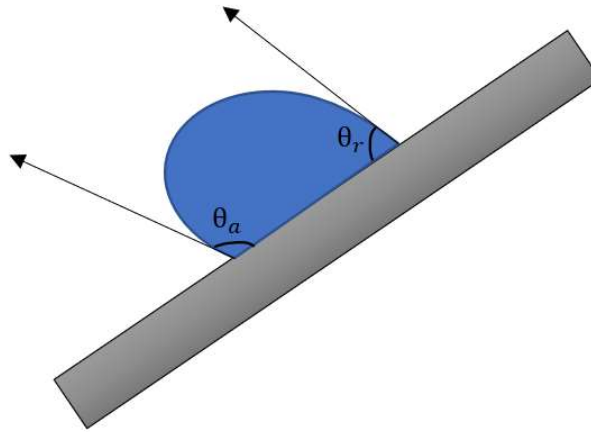
Figure 3. Contact angle hysteresis

The contact angle at the leading edge is called the advancing contact angle (θ_a), while that at the trailing edge is the receding contact angle (θ_r). The difference between these two angles ($\Delta\theta = \theta_a - \theta_r$) is defined as the contact angle hysteresis (CAH) which is another important parameter pertaining to a droplet-surface combination. This difference in contact angles for a single drop arises primarily due to the pinning of the contact line due to imperfections on the surface. For an atomically smooth surface, the contact angle hysteresis is low ($< 5^\circ$) which leads to a better drop mobility on the surface [7]. For a rough surface, there are two states in which the droplets can rest on the surface as shown in Fig. 4. The first among them is called the Wenzel State in which the liquid goes inside the imperfections of the surface leading to droplet pinning to the surface. The drop in this state is more stable and has low mobility. On the other hand, in the second state which is called as Cassie State, the droplet rests above the imperfections with air pockets forming inside the imperfections. In this state, the droplet is less stable and more mobile than the Wenzel State [8]. To shed the droplets faster and improve DWC, it is

necessary to avoid the Wenzel state altogether or convert the droplets in the Wenzel state to the Cassie state by providing external stimulus. Passive techniques (surface coatings) which avoid the Wenzel State as well as active techniques (electric fields, vibrations) to reach the Cassie State and promote droplet shedding at lower volumes have been exhaustively researched and will be covered in the upcoming chapter.
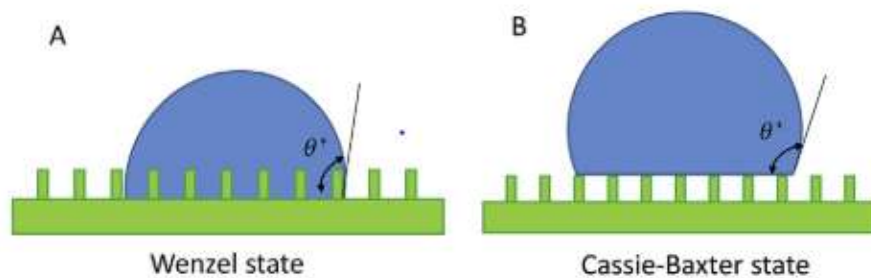
Figure 4. (A) Wenzel state and (B) Cassie state. Reprinted from [8]

CHAPTER II

LITERATURE REVIEW

DWC is a more efficient mode of condensation over film wise condensation. In DWC, the heat transfer coefficient is an order of magnitude higher than in FWC. However, in many industrial applications the main mode for condensation is still FWC since it is very hard to maintain stable DWC over the long term. Moreover, most surfaces used in heat exchangers are metals which are hydrophilic in nature, while DWC usually occurs on non-wetting surfaces. Drops nucleate at surface imperfections starting with a minimum radius depending on the condensing vapor, type of surface and level of subcooling as given by Equation 2. Further condensation causes the droplets to grow up till a critical radius (coalescence radius) given by Equation 3 before they coalesce with neighboring droplets to form larger drops. When the weight of the droplet overcomes the adhesive forces, the drop starts to slide. The radius at which this happens is called the maximum radius and is dependent on the static, advancing and receding angles of the droplet, and the surface tension of the liquid as given by Equation 4 [9].

$$r_{min} = \frac{T_{sat}\gamma}{h_{fg}\Delta T \rho} \tag{2}$$

$where\ \Delta T = T_{sat} - T_s$

$$r_e = (4N_s)^{-0.5} \tag{3}$$

$$r_{max} = \left(\frac{6\gamma(\cos\theta_r - \cos\theta_a)\sin\theta_e}{\pi\rho g(2 - 3\cos\theta_e + \cos^3\theta_e)}\right)^{0.5} \tag{4}$$

where ρ, g, γ is the density, acceleration due to gravity, and liquid-vapor surface tension respectively. T_{sat} and h_{fg} is the saturation temperature and latent heat of condensation of the fluid respectively while N_s is the nucleation site density on the condensing surface.

Zheng *et al*. [10] has summarized the work done by a lot of researchers to develop analytical solutions that show heat transfer through a single droplet. In that publication, it is shown that heat transfer through a droplet is directly proportional to the radius of the droplet, which suggests that droplets should be shed from the surface at a lower radius for better heat transfer performance. Also, various techniques that have been used to develop thin coatings on heat transfer surfaces, which render the surface hydrophobic (i.e., passive methods) are discussed. Apart from passive methods, others have used external forces (active methods) [11, 12] as well as a combination of passive and active methods[13-15] to improve DWC.

2.1 Passive techniques in DWC

2.1.1 Surface coatings

High droplet mobility can be achieved if the adhesive force between the surface and fluid is reduced or the contact angle hysteresis for a droplet on a surface is minimized. This can be done by altering the contact angle of the fluid on the surface either by applying hydrophobic coatings, ion implantation, fabricating micro-nano structures on surfaces, or making the surface slippery (atomically smooth). Due to the intrinsic water repellent nature of polymers, polymer coatings have been developed and tested to promote DWC. Holden *et al*. [16] tested 14 different polymer coatings on metal tubes and reported a heat

transfer coefficient 5-8 times higher than for FWC, durable over long times. However, for the coating to be durable, its thickness should be greater than 5 μm, which in turn impedes heat transfer [10]. Furthermore, Ma *et al.* [17] showed that nano-scale pin holes in polymeric coatings cause blistering, which can lead to the eventual degradation of the coating. Self-assembled monolayers (SAMs) have been shown to significantly enhance DWC performance [18-20]. SAMs are single layers of long chain molecules, which form by reacting with the surface to form strong chemical bonds with the other end having a low surface energy functional group, which renders the coated surface hydrophobic [10]. However, SAMs face durability issues due to the desorption from the surface either directly or by oxidation [21]. Rare earth oxides (REO) have been used to develop functional coatings since they become hydrophobic with hydrocarbon absorption as shown by Preston *et al.* [22]. Thermal and mechanical tests on REO show a robust behavior and 5X improved heat transfer performance as compared to other hydrophobic surfaces [23]. Similar results have been obtained using graphene coatings deposited via chemical vapor deposition [24], ion implanted metal surfaces, where carbon, nitrogen and oxygen ions were used [25, 26], and noble metals [27]. However, ion implantation is expensive while REO and noble metals need to replenish their absorbed surface contaminants to maintain a stable DWC [28, 29]. Since a high nucleation rate is important for improved DWC rate, which hydrophobic surfaces do not usually depict, patterned hydrophilic – hydrophobic surfaces (biphillic/hybrid surfaces) have been fabricated. The hydrophilic portion contributes to increasing nucleation rate while the hydrophobic region improves droplet mobility [10]. Yao *et al.* [30] demonstrated the wetting behavior of condensing droplets

on hybrid surfaces. They concluded that surface morphology of the hybrid surfaces has a strong influence on the final wetting behavior of the droplets. Furthermore, they proposed a surface-energy based model to predict wetting transitions and that could be potentially used to design hybrid surfaces. DWC rates greater than that on completely hydrophobic surfaces have been obtained after optimizing the hydrophilic-hydrophobic pattern on hybrid surfaces [31, 32]. Recently, stable DWC has been achieved on completely hydrophilic surfaces having low contact angle hysteresis ($<3°$), which proves that contact angle hysteresis has a significant effect on DWC more than its contact angle [33].

2.1.2 Micro-nano structured and slippery surfaces

Another method to induce low contact angle hysteresis is to fabricate micro/nano structured superhydrophobic (SCA $> 150°$) surfaces. If the surfaces are designed and tested with the proper structure geometry and level of subcooling, the droplets form on the surface in the Cassie State [34]. Furthermore, droplet coalescence on these surfaces can lead to the self-propelled droplet jumping phenomenon, if the released surface energy is more than the energy dissipated due to adhesive forces. This excess energy is converted to kinetic energy resulting in out-of-plane jumping of the droplet, thus leading to a faster droplet removal process [35]. Heat transfer experiments using nanostructured surfaces have shown up to 125% increase in DWC heat transfer coefficients [36]. However, increased subcooling leads to very small droplets nucleating inside the nanostructures, which can cause the surface to lose its super-hydrophobicity [37]. Furthermore, in the Cassie state, the air pockets between the droplets and the base surface could impede the

heat transfer process. To eliminate this issue and still maintain a low contact hysteresis, slippery liquid-infused porous surfaces (SLIPS) have been fabricated. The low surface energy liquid/lubricant fills the air pockets on the super-hydrophobic surface making the effective surface extremely smooth and water repellent [38]. DWC of steam on SLIPS in presence of NCGs was shown to have 100% higher heat transfer as compared to flat hydrophobic surfaces [39]. However, SLIPS are not durable due to lubricant depletion from the surface within a few hours [40].

2.2 Active techniques in DWC

2.2.1 Electrohydrodynamic fields (EHD) and electrowetting

Application of electric fields to improve two-phase heat transfer processes like condensation and boiling have been studied since the last 30 years. The condensation is improved due to the electrostatic force applied on the fluid by the external electric field [41]. According to an exhaustive review conducted by Laohalertdecha *et al.* [12], the mechanisms responsible for condensation enhancement due to EHD are as follows

- Thinning of condensate film due to the liquid forced away from the condensation surface due to the electric field

- Changing of FWC to pseudo-DWC

- Dispersion of condensate film due to electrostatic atomization

- Lesser accumulation of non-condensable gases at the liquid vapor interface

- Inducing waviness in the condensate film

In one of the early works by Velkoff and Miller [42] in application of EHD to improve condensation of Freon-113 on vertical surfaces, a heat transfer enhancement of 150% was achieved using an electric field perpendicular to the cooled copper plate. Later, Choi [43] showed that the increase in heat transfer was due to the instability waves at the liquid film interface which reduced the average film thickness of the liquid. Didkovsky and Bologa [44] obtained a 20X increase in the condensation heat transfer coefficient for dielectric fluids on cooled vertical copper surfaces under EHD. This rise was attributed to the reduction in film thickness due to spraying of the condensate into the vapor phase and transverse wave formation at the liquid – vapor interface. EHD requires a fluid with low electrical conductivity like refrigerants [45]. Thus, water cannot be condensed efficiently using EHD.

Electric fields have further been used in tandem with the droplet jumping phenomena to improve dropwise condensation by preventing the droplets which jumped, to return to the surface [14]. Electrowetting is a technique used to alter the wetting behavior of liquids on metal surfaces coated with a dielectric material. Applying a potential difference across the dielectric creates an electric double layer with charges from the metal on one side and an equal opposite charge on the liquid side, which alters the interfacial tension [46]. It has been shown that due to Electrowetting in AC electric fields (AC – Electrowetting), the condensate droplets shed faster due to lower contact angle hysteresis and improved coalescence [47]. Recent condensation experiments conducted by E. Wikramanayake *et al.* [48] leveraging the AC - Electrowetting phenomena has shown a 31% improvement in condensation rates.

2.2.2 Bulk vibrations

As discussed earlier, a low CAH is crucial for high droplet mobility on an inclined surface. Given the shortcomings in developing smooth coatings, it is necessary to find alternative ways to achieve a low CAH or overcome the pre-existing CAH. It has been shown that CAH can be looked at from the perspective of an energy barrier to droplet motion, which occurs due to droplet pinning on surface imperfections [49]. Rahimzadeh et al. [50] conducted high frequency vibration experiments (i.e. around 40kHz) with droplets, which showed that the maximum pinning forces on the droplets are given by Equation 5 and can be related to the potential energy barrier given by Equation 6.

$$F_{pin}^{max} = \gamma_{LV} cos(\theta_r) + \gamma_{SL} - \gamma_{SV} \qquad (5)$$

$$U = F_{pin}^{max} \delta r \qquad (6)$$

where, δr is the elemental displacement of the contact line and F_{pin}^{max} is the maximum pinning force per unit length. The droplet will be able to move on the surface if the depinning forces are greater than the pinning forces which can be accomplished by imposing vibrations.
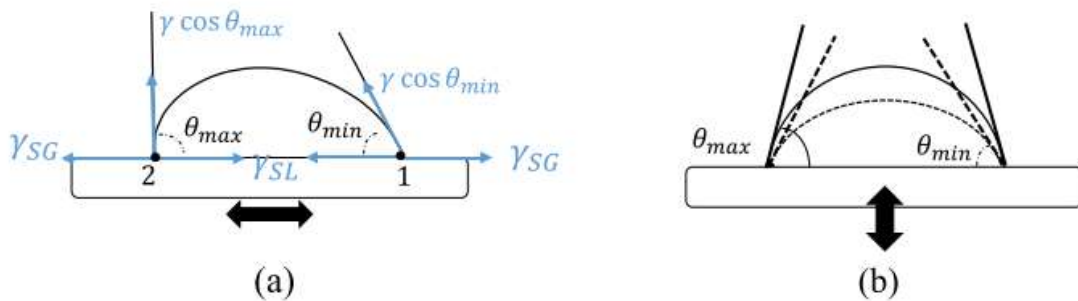
Figure 5. (a) Lateral vibration (b) Longitudinal vibration. Reprinted from [50]

There are two types/directions in which vibrations can be provided to the surface and in turn to the drop resting on it, namely longitudinal and lateral vibrations. As shown in Fig. 5, the droplet moves vertically increasing and decreasing in height on imposing longitudinal vibrations. The left and right contact angles (diametrically opposite points) oscillate in phase and undergo a minimum and maximum simultaneously for small droplets. Both the contact lines, undergo a maximum and minimum depinning force together, in small droplets. During lateral vibrations, the droplet undergoes a rocking motion where the left and right contact angles oscillate, one reaching maximum advancing angle on one front, while the other reaches minimum receding angle on the other front. When one contact line is undergoing a maximum depinning force, the other is undergoing a minimum. These forces per unit length are given by Equations 7 and 8.

$$F_1 = \gamma_{LV} cos(\theta_{min}) + \gamma_{SL} - \gamma_{SV} \tag{7}$$

$$F_2 = \gamma_{LV} cos(\theta_{max}) + \gamma_{SL} - \gamma_{SV} \tag{8}$$

where, θ_{max} and θ_{min} are the maximum and minimum contact angles during vibration and 1 and 2 are diametrically opposite points as shown in Fig. 5 (a). F_1 and F_2 are force per unit length on the receding and the advancing front of the droplet respectively. This imbalance in the force per unit length ($F_1 > F_2$) on diametrically opposite points on the droplet, while vibrations are imposed would lead to drop motion.

2.2.3 Drop motion under longitudinal vibrations

Andrieu *et al*. [51] used longitudinal vibrations at 50Hz and amplitudes varying from 0.3 to 2.5 mm, to unpin the droplets from surface defects ranging from 4 μm to 0.1

mm and calculated the mean spreading parameter. They found that the contact angle hysteresis decreases as amplitude of vibration increases and proposed that the unpinned static contact angle is given by Equation 9.

$$cos(\theta_e) = \frac{cos(\theta_a) + cos(\theta_r)}{2} \tag{9}$$

Boryeko and Chen [52] imposed longitudinal acoustic vibrations on droplets placed on superhydrophobic surface and observed a Wenzel to Cassie transition in the droplet state for millimetric drops. They tested frequencies ranging from 15 – 150 Hz for a 1.5 µL droplet to gauge the threshold amplitude for this transition to occur. They found two frequencies, which give local minima for the threshold amplitude and concluded that these frequencies were the first and second resonance modes of the drop.

Brunet *et al.* [53] performed experiments on droplets on inclined surfaces under vertical vibrations. Since the substrate was inclined, the droplet experienced both longitudinal and lateral vibrations. They showed that for different accelerations and frequencies imposed on the substrate, the droplet can either remain static (pinned) on the surface, slide down the incline or climb up the incline as shown in the phase diagram in Fig. 6. The first resonance mode frequency $(f_o = 50.77Hz)$ was chosen as the normalization factor for the frequency and the corresponding acceleration given by $a_o = (2\pi f_o)^2 A$, where A is the amplitude of vibration, as the normalization for acceleration.
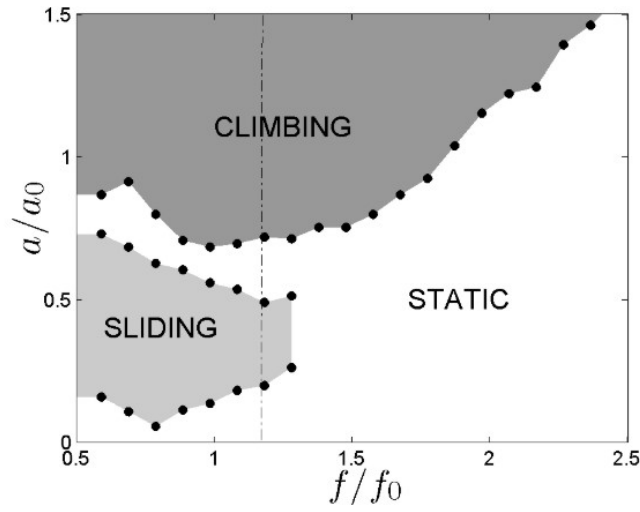
Figure 6. Effect of vibration frequency and acceleration on droplets. Reprinted from [53]

Further, they performed the same experiment for droplets placed on a horizontal surface and subjected to an acceleration angled away from the surface as shown in Fig. 7 to prove that shaking always produces an upward motion irrespective of gravity. This motion was attributed to the unbalanced young's capillary forces acting on the contact lines of the droplet. Sartori *et al.* [54] performed similar experiments for droplets having a range of kinematic viscosities and surface tensions. They got similar phase diagrams as got by Brunet *et al.* [53] and found that kinematic viscosities in the range of $1 - 39 \frac{mm^2}{s}$ do not significantly affect the phase diagram shown in Fig. 6. However, low surface tension fluids were found to favor sliding over climbing.

16

Figure 7. Drop on a horizontal plate shaken at an angle. Reprinted from [53]

From past studies, it is clear that resonance frequencies of droplets subjected to external vibrations are important with regard to drop mobility on a surface. One of the very early works in determining resonance frequencies for drops was done by Lamb [55]. He developed an expression given by Equation 10 to determine resonance modes (Rayleigh Modes) of a free liquid droplet undergoing small-amplitude vibrations neglecting viscous effects.

$$\omega_j^2 = \frac{j(j+1)(j-1)(j+2)\gamma}{((j+1)\rho + j\rho^e)R^3} \tag{10}$$

where, ρ, ρ^e *and* R are the density of the fluid droplet, density of the surrounding fluid and the radius of the droplet respectively while, j is any integer greater than or equal to 2 and is the mode number of vibrations. Later Strani and Sabetta [56] discovered that drops in partial contact with a solid surface have an extra vibration mode (rocking mode) at lower frequencies which is absent in free drops. They also showed that the solid support could slightly increase the resonant frequencies of the Rayleigh modes.

Since resonance frequencies typically depend on the radius of the droplet, it is important to estimate the radius of the drop accurately. Quere [57] studied static drops

placed on horizontal and vertical surfaces. He developed an expression for the radius at the belly of the droplet as given by Equation 11. Further, he also gave a threshold droplet volume at which the droplet would slide from a vertical surface as a function of contact angle concluding that the sliding usually happens when the drops are often large as compared to the capillary scale.

$$R = \left(\frac{3V}{\pi(1 - cos\theta_e)^2(2 + cos\theta_e)}\right)^{1/3} \tag{11}$$

where, V is the droplet volume.

Noblin *et al.* [58] studied the resonance modes of droplets undergoing longitudinal vibrations with the amplitude varying with time following a cosine function. They observed two types of vibrations, one with a pinned contact line and the other with a mobile contact line at low and high amplitudes respectively. For the first type (pinned contact line), the resonance modes were attributed to stationary surface waves and Equation 12 was developed to predict the corresponding resonance frequencies.

$$\omega_j^2 = \left(g q_j + \frac{\gamma}{\rho} q_j^3\right) \tanh\left(q_j \frac{V}{\pi R^3}\right) \tag{12}$$

$$where, q_j = \frac{\pi(j - 0.5)}{p}$$

where, $p = R\theta_e$ is the arc length of the droplet from the center to the edge. Further, when they increased the amplitude, the droplet experienced mobile contact line oscillations since the variation of contact angles exceeded the contact angle hysteresis. For each drop size and imposed frequency, they found a threshold amplitude for which the contact line moves.

2.2.4 Drop motion under lateral vibrations

One of the early studies on drops subjected to lateral vibrations was done by Daniel *et al.* [59] where they analyzed drop motion on surfaces having a wettability gradient. If the contact angle hysteresis is negligible, drops tend to move to areas having a high wettability to achieve an overall minimum surface energy. However, when the contact angle hysteresis is significant, the drop must overcome the hysteresis by means of external forces. By imposing lateral vibrations to surfaces having a wettability gradient, they found that drops can overcome the contact angle hysteresis and start to move. Furthermore, it was found that the velocity of the drops increased linearly with increasing amplitude and when the forcing frequency was equal to either the first or the second Rayleigh mode. Work on surfaces having a thermal gradient, culminating in similar results, was conducted by Mettu *et al.* [60].

To build on Strani and Sabetta's work, Celestini *et al.* [61] worked on fully characterizing the fundamental vibration mode for a supported droplet. They developed an expression for the fundamental (rocking) mode using a simple oscillator model given by Equation 13.

$$\omega_o = R^{-\frac{3}{2}} \sqrt{\frac{6\gamma h(\theta_e)}{\rho\left(1 - cos(\theta_e)\big(2 + cos(\theta_e)\big)\right)}} \tag{13}$$

Here, $h(\theta_e)$ was calculated numerically based on the hypothesis that the initial deformation of the drop in the oscillator model minimizes the free energy of the drop under

the influence of external vibrations. $h(\theta_e)$ was found to be dependent on the wetting angle as shown in Fig. 8 but material independent.
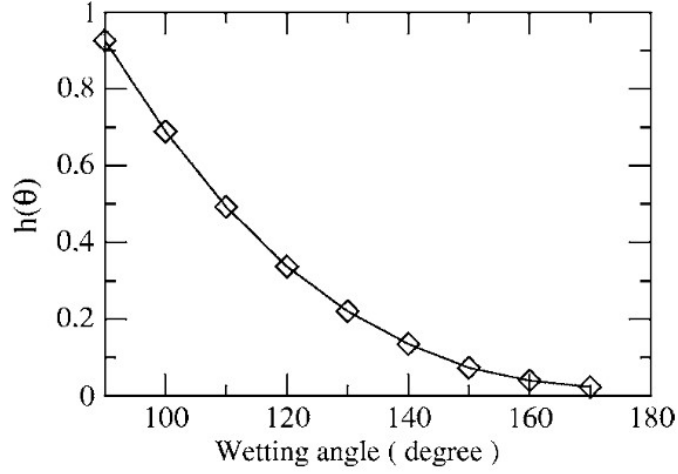
Figure 8: Numerical values for h(θ) used in Equation 13. Reprinted from [61]

For a supported drop vibrated via surface vibrations, the momentum is transferred through a small distance within the fluid, near the surface, called the Stokes length given by Equation 14

$$\delta = \left(\frac{2\mu}{\omega}\right)^{0.5}$$ (14)

where, μ is the dynamic viscosity of the fluid. They further proposed a first order correction for the true equilibrium contact angle in the limit of small Stokes length as given by Equation 15.

$$\theta_{eff} = \theta_e - \frac{\delta}{R sin(\theta_e)}$$ (15)

Apart from developing the model, the authors also conducted experiments on mercury drops placed on glass undergoing lateral vibrations and found a good agreement with the model predictions.

Daniel *et al.* [62] studied drop motion under lateral vibrations for drops on horizontal silicon wafers coated with a self-assembled monolayer of alkyltrichlorosilane, regarding batch microfluidic processes. They identified the resonance frequencies for the rocking mode and higher order modes for different droplet volumes ranging from 1 – 10 µL and expressed it as a function of droplet mass as shown in Fig. 9.
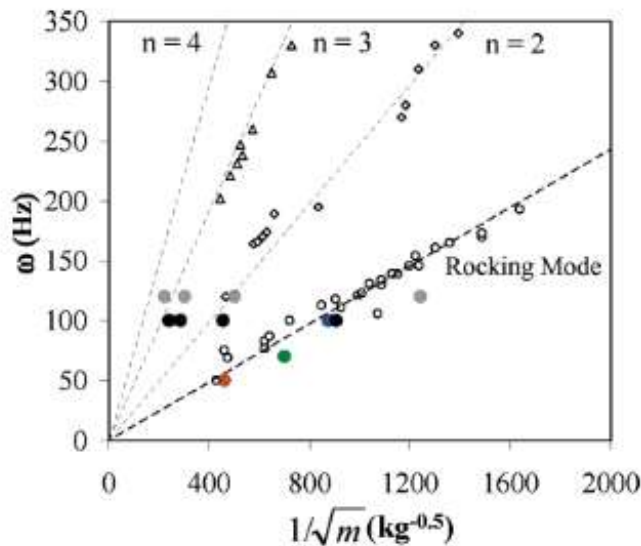
Figure 9. Resonance frequency as a function of droplet mass. Reprinted from [62]

Sharp *et al.* [63] conducted experiments to estimate the resonance frequencies as a function of static contact angle for microliter sessile water droplets sitting on a horizontal surface. They developed a model to predict resonant frequencies (including the rocking mode) which has a similar form as Equation 10 with j = 2 corresponding to the rocking

mode. They provided detailed plots for the square of the fundamental resonant versus the reciprocal of droplet mass for different surfaces as shown in Fig. 10. Furthermore, they also found that the slope from Fig. 10 can be correlated to the static contact angle as shown in Fig. 11.
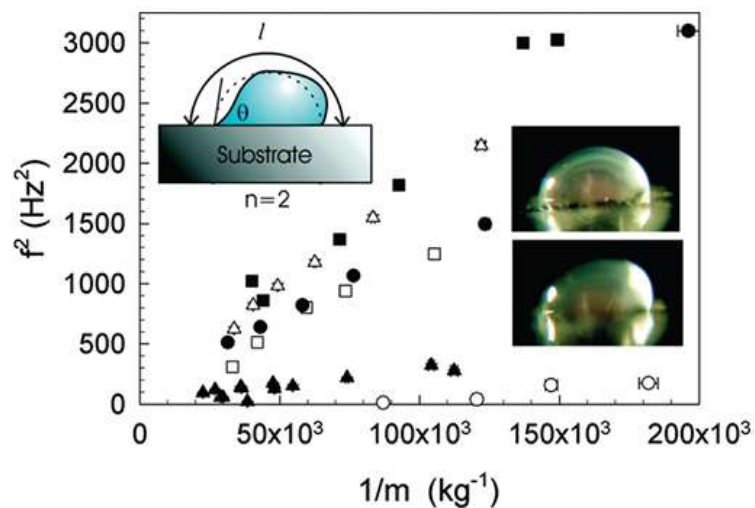
Figure 10. Resonance frequency as a function of drop mass for different surfaces. Data for glass (○), silicon (□), PMMA (△), PS (■), PDMS (●) and hydrophobic sand (▲). Reprinted from [63]
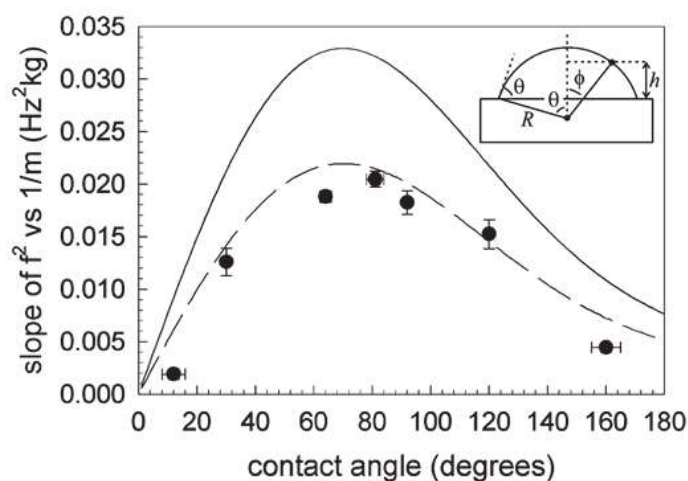
Figure 11. Contact angle dependence of fundamental mode resonance frequencies. Reprinted from [63]

Dong *et al.* [64] performed numerical simulations to identify the resonance modes of a drop placed on a hydrophobic surface undergoing lateral vibrations. The vibration of the drop near the surface was caused due to momentum diffusion in the Stokes layer. Beyond the Stokes layer, the inertial force, and the restoring force due to Laplace pressure cause capillary waves on the drop surface giving rise to different resonant modes. The authors also analyzed different modes of drops placed on vertical surfaces undergoing lateral vibrations. An important observation from their study was that gravity enhances the first resonant mode or the rocking mode and weakens the second mode.

Yao *et al.* [65] conducted experiments on droplets placed on hybrid surfaces undergoing both lateral and longitudinal vibrations. They found the first and second mode resonance frequencies for 5, 10 and 15 μL droplet volumes and studied the effects of those frequencies on the sliding angle of the droplet. They found that smaller droplet volumes exhibit a significant lateral motion as compared to larger droplet volumes at their respective first mode resonance frequencies. Furthermore, it was found that first mode

23

resonance frequencies have lower sliding angles as compared to second mode resonance frequencies, which prove that the rocking mode is more effective in overcoming the contact angle hysteresis.

Huber *et al.* [66] conducted simulations and experiments on a 2.6mm-diameter water drop placed on a vertical surface. Both, longitudinal and lateral vibrations were provided to the drop. It was observed that the drop underwent four motions, rocking, ratcheting, ratcheting with break up and ejection. In the rocking mode the contact line remained pinned, which was observed at low accelerations. Increasing the acceleration above a threshold, caused the drop to transition into a ratcheting motion. The rocking and ratcheting motion depended only on the lateral component of the vibration while a combination of both kinds of vibrations led to droplet ejection.

Recently, Sakakeeny *et al.* [67] conducted simulations for studying the effect of Bond number on lateral oscillation frequencies for supported drops with pinned contact lines. They found that droplet oscillation frequencies vary significantly with Bond number (Bo) even when the drop size is less than the capillary length. Furthermore, they found that the resonance frequency decreases with Bo for droplets on vertical surfaces, while the opposite trend is observed for droplets on horizontal surfaces. In their next publication [68], they provided an analytical expression given by Equation 16 to predict the oscillation frequency for droplets with a pinned contact line, placed on vertical surfaces, as a function of the Bo and static contact angle. A part of this thesis work was used to experimentally validate their model and as revealed from the publication, a good agreement between the experiment, simulation and model was seen.

$$\frac{\omega^2}{\omega_c{}^2} = \frac{12\left(\eta + \frac{3\xi}{2\eta^2}Bo_1^2\right)}{\zeta(2 + cos\theta_e)(1 - cos\theta_e)} \tag{16}$$

where,

$\eta = a_o\left((\exp(a_1 cos\theta_e + 1) - 1\right)$ is the coefficient of the second order displacement term

$-\xi = b_o\left((\exp(b_1 cos\theta_e + 1) - 1\right)$ is the coefficient for the fourth order displacement term,

$\zeta = c_1\left(\left(erf(\frac{cos\theta_e+1}{c_2})\right) + 1\right)$ is the kinetic energy correction factor

$$Bo_1 = \frac{0.42(2 + cos(\theta_e))^{\frac{1}{3}}}{(1 - cos(\theta_e))^{\frac{-1}{3}}}Bo \; ; Bo = \frac{\rho g R_d}{\gamma} \; ; R_d = \left(\frac{3V}{4\pi}\right)^{\frac{1}{3}}$$

$\omega_c = \sqrt{\frac{\gamma}{\rho R^3}}$ is the capillary frequency

where, V is the droplet volume, θ_e is the static contact angle of the droplet with the surface and R is given by Equation 11.

2.2.5 Condensation with vibrations

Condensation improvement with vibrations imposed on the evaporator in saline water conversion systems, was first observed by Raben et. al. [69] at Southwest Research Institute. They found that above a cut-off intensity, heat transfer coefficients increase with increasing vibration intensities and up to a maximum of 55% as compared to the without vibration case. Dent [70] conducted experiments on steam condensation on horizontal tubes vibrating in the frequency range of 20-80 Hz with maximum amplitudes up to 4.3

mm. He found that condensation heat transfer coefficients increase with vibration intensity up to a maximum of 15% as compared with the vibration-free case. In his second paper, he developed a model to predict heat transfer coefficients for FWC on a vertical tube undergoing transverse vibrations [71].

After Dent's work in 1969, the study on condensation enhancement using vibrations has recently gathered a lot of interest, mostly due to the lack of durability of coatings used as passive techniques to improve DWC. Zhang *et al.* [72] observed the droplet distribution during DWC on a PVC coated aluminum surface subjected to ultrasonic vibrations of different powers. They concluded that with ultrasound the shedding of droplets is accelerated and increases even more as the power of the vibrations is increased. Furthermore, the heat flux and heat transfer coefficients both increase with ultrasonic power. Migliaccio [11] studied the effects of mechanical vibrations in the range of 100 – 400 Hz on DWC on vertically oriented surface. He observed appropriately sized drops resonating and shedding off at lower volumes and at a higher rate than for the stationary case, and thus reported a 70% increase in heat transfer over vibration-free DWC. Tong *et al.* [73] investigated the effects on low frequency *(~ 10^2 Hz)* and high acceleration (~10^3 m s^{-2}) vibrations on a surface with a hydrophobic coating. They found a reduction in thermal resistance between 5.2% - 21.9% due to the combined effect of surface hydrophobicity and vibrations as compared to a hydrophilic and vibration free case.

Huber and Derby [74] conducted DWC experiments on stationary Teflon films in comparison to vibrating Teflon films at 100 Hz. Apart from the conclusions seen from

previous studies, they concluded that vibrations increased the rate of droplet coalescence. Moradi *et al.* [15] recently conducted experiments where they imposed longitudinal vibrations on condensing droplets. They found that constant frequencies in the range of 60 – 160 Hz do not lead to significant heat transfer improvement since only a few droplets were found to resonate. They used cyclic frequencies with a peak of 132 Hz to mechanically vibrate a superhydrophobic surface experiencing DWC and reported a 15% increase in condensation. Oh *et al.* [13] recently studied the effects of vibrations for DWC on Slippery Liquid Infused Surfaces (SLIPS) and reported a 40% increase in heat flux. Furthermore, they achieved a 39% smaller drop departure size and 8x faster shedding speeds as compared to DWC on non-vibrating SLIPS that led them to propose improved water harvesting as a potential application.

2.3 Summary of literature review

To promote dropwise condensation over film wise condensation, it is essential to reduce the drop departure size. A low contact angle hysteresis and large static contact angles leads to a better drop mobility on the surface and are the main factors which lead to a small drop departure size. These conditions can be achieved by fabricating engineered surfaces (passive techniques) or can be overcome using external forces (active techniques). Surface modification techniques like polymer coatings, self-assembled monolayers, ion implantation, rare-earth oxides and noble metal coatings have been used to improve DWC rates. Hydrophilic-hydrophobic patterned surfaces which have improved nucleation in the hydrophilic region and improved droplet shedding in the hydrophobic

27

region have been fabricated to improve DWC. Furthermore, micro-nano textures, which render the surface superhydrophobic and improve droplet shedding have been fabricated as well. Moreover, Slippery Liquid Infused Surfaces (SLIPS) have been fabricated on which drops experience ultra-low contact angle hysteresis and thus are highly mobile. However, most of the passive techniques have their own shortcomings including poor mechanical and thermal integrity of coatings, which are not durable. Thus, it is necessary to shift focus to active techniques. As presented above, application of electrohydrodynamic fields for polar and non-polar fluids lead to thinning of the condensate film on the surface and have been used to improve the rate of film wise condensation. Electro-wetting uses a dielectric layer having a voltage difference between the surface and the droplet, which changes the wetting behavior of the fluid. Electrowetting has been used to improve dropwise condensation rates and seems promising. Longitudinal and lateral bulk surface vibrations have been shown to be useful to overcome contact angle hysteresis. When the drop is pinned, it experiences different resonance modes (Rayleigh modes) due to the surface waves caused by the imbalance in the inertial and restoring forces. For supported drops, there is one more resonance mode (rocking mode), which occurs at low frequencies which is absent for free drops. The drop usually starts to move on a surface above a threshold amplitude. The velocity of the drop increases with amplitude and reaches a maximum when the forcing frequency is equal to the resonant modes of the droplet. For drops placed on vertical surfaces under lateral vibrations, gravity enhances the rocking mode which could lead to improved dropwise condensation. It has been shown that the sliding angle for droplets placed on hybrid

28

surfaces undergoing both lateral and longitudinal vibrations is less for first resonance mode as compared to the second resonance mode. This suggests that for effective droplet sliding the droplet should be imposed with the rocking mode resonance frequency. After a couple of studies during the early and late 1960's, interest in vibration induced condensation has recently been renewed. Experiments have been conducted to study condensation behavior with and without vibrations for both longitudinal and lateral vibrations. DWC improvements up to 70% have been achieved with vibrations as compared to non-vibrating cases.

2.4 Research gaps and study objectives

2.4.1 Research gaps

Various experimental and numerical studies [55, 56, 61] have been conducted to develop a model for the resonance frequencies of sessile microliter water droplets. Experimental studies were also conducted by Sharp *et al.* [63] and Daniel *et al.* [62] to estimate resonance frequencies for different modes as a function of droplet mass and static contact angle. However, the studies mentioned above consider droplets on horizontal surfaces where the Bond number is practically zero when gravity does not play a significant role. Moreover, there have been limited studies which have delved into studying droplets vibrating laterally on vertically oriented surfaces. Previous studies [52, 53, 58, 66] show that there is a threshold vibration amplitude for the droplets to become mobile on the surface. One of those studies [52] in which, the Wenzel to Cassie transition on horizontal superhydrophobic surfaces was studied, shows that minimum amplitudes are required for this transition at first and second modes of the imposed longitudinal

vibrations. Furthermore, it was also shown that after the droplet was set in motion on horizontal surfaces, the linear velocity of the droplet reaches a maximum when the frequency is equal to the rocking mode resonance frequency [62]. However, there are limited studies, which systematically quantify the effect of resonant vibrations on droplet mobility on vertical surfaces. Such studies, if conducted, can help expedite the droplet shedding process with the least amount of input energy. One such application where fast droplet shedding is of the essence is dropwise condensation. There are very limited studies on dropwise condensation in the presence of vibrations. Some of the studies, show the effects of longitudinal vibrations on dropwise condensation [15, 74]. Other studies which impose lateral vibrations on the surface during dropwise condensation, have studied its effects at high frequencies ($\sim 10^2$ Hz) [11, 73] or at frequencies in the ultrasonic range [72]. Moreover, most of the studies mentioned above consider hydrophobic surfaces with contact angles more than 100º and just apply control on the frequency of vibrations and not on the amplitude. Furthermore, even though Migliaccio [11] considered the input energy for lateral vibration during DWC, there was no particular reason given for choosing the corresponding frequencies and amplitudes. Proper selection and control on amplitude and use of lower frequencies are necessary to quantify and optimize the amount of input energy provided to the system, which is important to determine the overall net effect on system performance. Dropwise condensation both in presence of low frequency ($< 10^2$ Hz) lateral vibrations and on hydrophilic and hydrophobic surfaces (contact angle < 90º) with a precisely controlled frequency and amplitude for the vibrations is yet to be studied.

2.4.2 Study objectives

In a previous study [64] on simulations of droplets on vertical surfaces vibrating laterally, it was shown that gravity enhances the rocking mode and weakens the other modes. Furthermore, as seen from the previous section, there is a need to systematically address the effect of finite Bond number by estimating the resonance frequencies for vertically oriented surfaces. Thus, the first objective of this study is to identify and quantify the resonance frequency of the rocking mode for drops placed on vertically oriented surfaces. The second objective of this study is to estimate the effect of resonant vibrations on the mobility of droplets on vertically oriented surfaces under different vibration conditions (i.e., different acceleration values). Furthermore, the effect of frequencies away from resonant frequencies on drop mobility should also be considered. The final objective of this thesis work is to study the effects of low frequency resonant vibrations on dropwise condensation under controlled conditions including prescribed amplitudes of vibrations. Furthermore, the effects of resonant vibrations on different surface types (hydrophobic and hydrophilic) should also be investigated.

CHAPTER III

EXPERIMENTAL SETUP AND METHODOLOGY

3.1 Experimental setup for droplet wetting experiments

The first two parts of the thesis work, termed as droplet wetting experiments, consisted of identifying resonance frequency and sliding threshold amplitude for a single droplet. The goal of the wetting experiments was to study the effect of vibration frequencies and amplitudes on sessile microliter DI water droplets. An experimental set-up was designed as shown in Figures 12 and 13. The setup consisted of a speaker- amplifier system, high speed camera, data acquisition system, accelerometer, accelerometer power supply, backlight illumination, a vertical stand to support the surfaces, and a computer. A pneumatically damped optical table was used to conduct all wetting experiments to reduce noise from ambient sources.
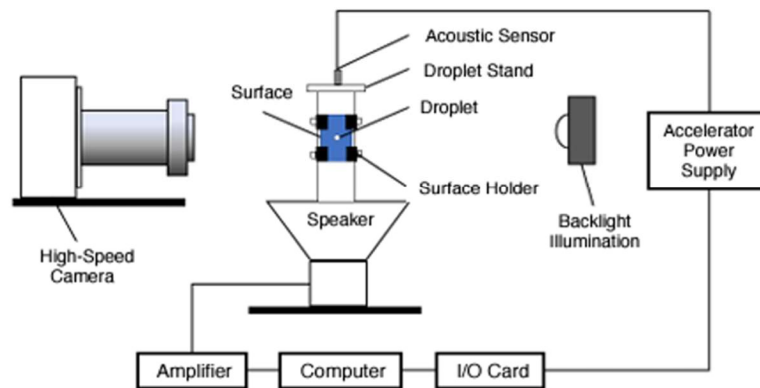
Figure 12. Schematic of the experimental setup for droplet wetting experiments. Adapted from [75]
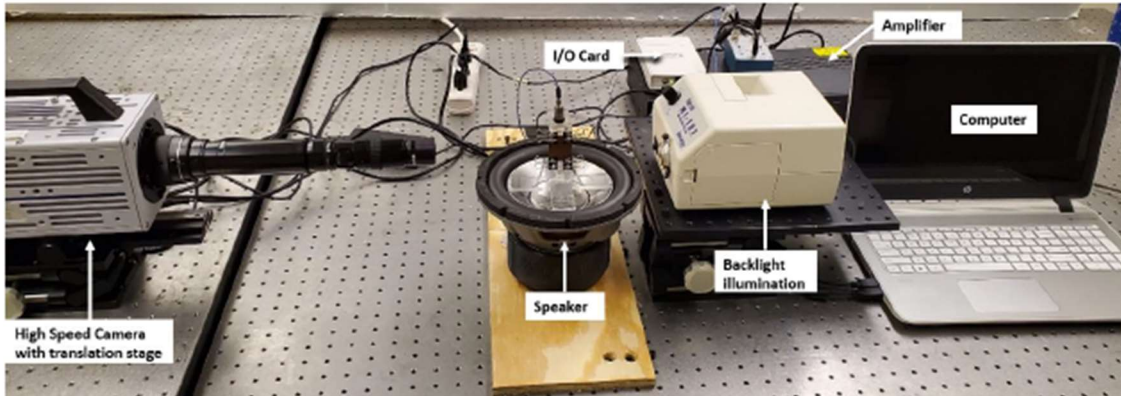
Figure 13. Actual setup for droplet wetting experiments. Reprinted from [75]

3.1.1 Substrates

Five commercially available substrates, i.e., aluminum, copper, polystyrene, PTFE, and wax were used for the wetting experiments. The dimensions of each surface were 28 mm × 28 mm. Mirror – polished aluminum 6061, PTFE (McMaster-Carr) and copper 110 (MSC Industrial) were cut from their respective 1.59 mm thick sheets. Polystyrene was cut from a 3.18 mm thick polystyrene sheet supplied by McMaster-Carr. The wax surface was fabricated in-house by attaching wax paper on a polystyrene surface by spray glue.

3.1.2 Substrate stand

A stand to support surfaces vertically was fabricated from PMMA to minimize weight of the system as shown in Fig. 14. All parts in the stand were attached together after ensuring that they were perfectly horizontal with the help of a level. The substrate stand was attached to the upper rim of the speaker with the help of a level to ensure a

perfectly horizontal attachment. Furthermore, a plate on top of the substrate stand was used to attach the accelerometer to the system as shown in Fig. 15
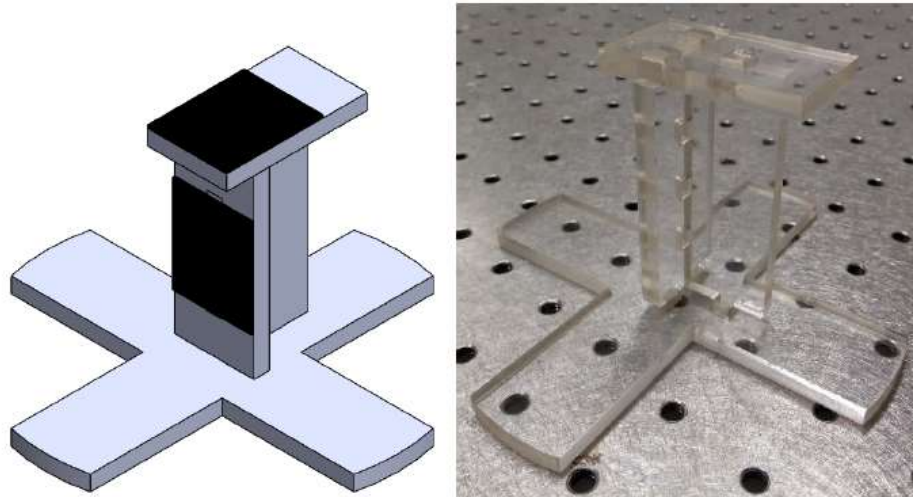
Figure 14. Substrate Stand. Reprinted from [75]
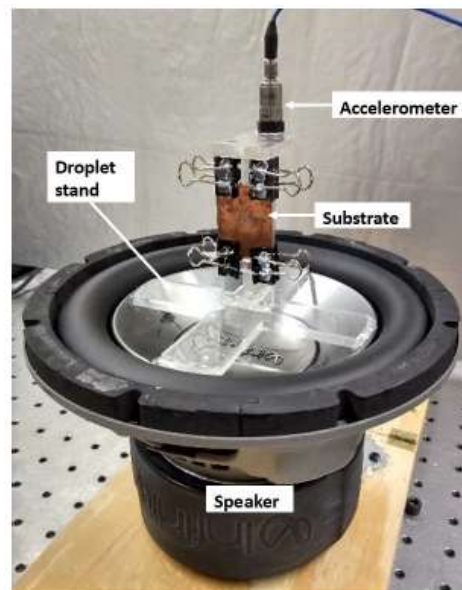
Figure 15. Speaker - substrate stand - accelerometer assembly. Reprinted from [75]

3.1.3 Speaker – amplifier system

A sound speaker (Infinity Reference 860 W, Infinity Inc.) as shown Fig. 16 was attached to an amplifier (Russound P75-2 Channel Dual Source 75 W) as shown in Fig. 17. The amplifier was used to provide controlled amplitude lateral vibrations to the stand and the substrate. The frequency was provided and controlled using the Online tone generator [76]. The online tone generator is a freely available online tool which can provide vibrations at different frequencies at a sampling rate of 44.1kHz and of sine, square, sawtooth and triangle wave forms. Furthermore, it can provide frequency sweeps from an initial frequency to a final frequency for a specified time interval.

Figure 16. Sound Speaker, Infinity Inc.

Figure 17. Amplifier

3.1.4 Imaging system

A high-speed camera (Photron SA3) was used to capture images for both static and vibrating droplets as shown in Fig. 18. The camera can record up to 1000 frames per second with a resolution of 1024×1024 and up to 60,000 frames per second at reduced resolutions. The camera was placed on a translation stage to have good focus on the droplet. A halogen lamp (Fiber-Lite MI series, Dolan-Jenner Inc.) was used as an illumination source to aid the camera to capture images with a good contrast. The light was focused on the droplet using a focusing attachment at the source of the light.

Figure 18. High speed camera with translation stage

Figure 19. Halogen lamp for backlight illumination

3.1.5 Accelerometer and data acquisition system

An accelerometer (352C04, PCB Piezoelectronics) powered using a power supply (P5000, MISTRAS), was connected to the top plate of the substrate stand to measure vibration frequencies and accelerations of the substrate stand. The accelerometer had a sensitivity of 10 mV/g, acceleration measurement range of ±500 g, frequency measurement range of 0.5 – 10000 Hz (± 5%) and a resolution of 0.0005 g in the root mean square value for acceleration. A data acquisition system (NI USB-5132, National Instruments Inc.) was used to interface the accelerometer with the NI-SCOPE (National Instruments Inc.) software on the computer.

Figure 20. Accelerometer (352C04, PCB Piezoelectronics)

3.2 Methodology for wetting experiments

3.2.1 Contact angle measurement

Each droplet volume was placed on each horizontal surface using a micro-pipette. The micro-pipette was initially calibrated using a micro-balance with a resolution of 0.1 milligrams. To determine the contact angle of each droplet when sitting on a flat surface, images of each droplet were captured using the high-speed camera. The outline or silhouette of the image of a single droplet was extracted using the MATLAB's Canny Algorithm [77] with a threshold of 0.05. The threshold is a numerical value selected by the algorithm to ensure adequate signal to noise ratio in the image [78]. Moreover, if the point on the edge is above the threshold value, it is considered as an edge. Keeping the threshold low is helpful in identifying all the possible outlines of an image, while if the thresholds are kept to a high value there is a risk of missing some outlines. Furthermore, the downside of using very high thresholds is the possibility of high number of false positive outcomes for the outlines detected.

The contact angle was measured by importing the drop outline or silhouette using ImageJ [79] and using the 'Contact_Angle.jar' plugin in it. The process followed by ImageJ consists of placing an overall of 5 points on the outline of each drop. The first two points are placed at the two contact lines and the rest are placed on the drop outline as shown in Fig. 21. This is done for all the droplet volume-surface combinations used. Since the contact angle is typically independent of volume, the average of all the contact angles obtained for all volumes on a single surface was used for analysis purposes. The same

procedure was repeated when measuring advancing and receding contact angles for each droplet placed on vertically oriented surfaces.
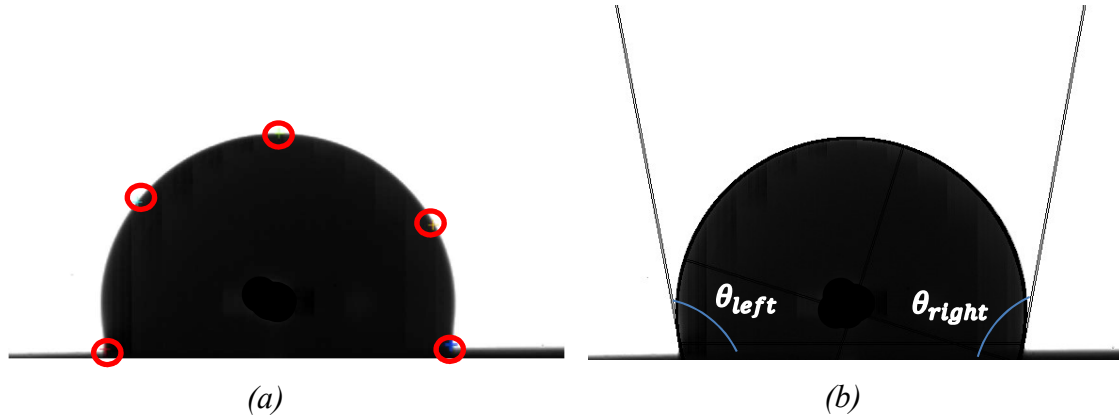
Figure 21. Contact angle measurement for *(a)* 4.78 μL droplet on PTFE with 5 points on the outline *(b)* left and right contact angles

3.2.2 Identification of resonance frequency of droplets on different substrates

To determine the resonance frequency of each droplet-surface combination, Celestini's equation [61] was used initially to estimate the corresponding resonance frequency. For all the resonance experiments the Celestini's equation was used as a starting point in increments/decrements of 5 Hz. For each frequency tested, 100 droplet images were captured at 500 frames per second and the outlines of all the images were superimposed on one another as shown in Fig. 22. The outlines were extracted using the Canny algorithm of MATLAB [77] with a threshold of 0.05. From the image of the superimposed outlines, the coordinates of the droplet center (x_c, y_c) for all cases are at the same position, where x_c is same as the x-coordinate of the base of the droplet, while y_c is calculated as the average of the y-coordinate of the two contact lines as shown in Fig. 22

(a). The distance between the center of the droplet and the droplet edge was found by using Equation 17.

$$D = \sqrt{(x - x_c)^2 + (y - y_c)^2} \tag{17}$$

where (x, y) are the pixel coordinates of any point on superimposed droplet outlines.

The outline passing through the point having the maximum distance (D) from the center of the droplet was used to determine the advancing and receding contact angles using ImageJ as explained in Fig. 23.

(a)   *(b)*
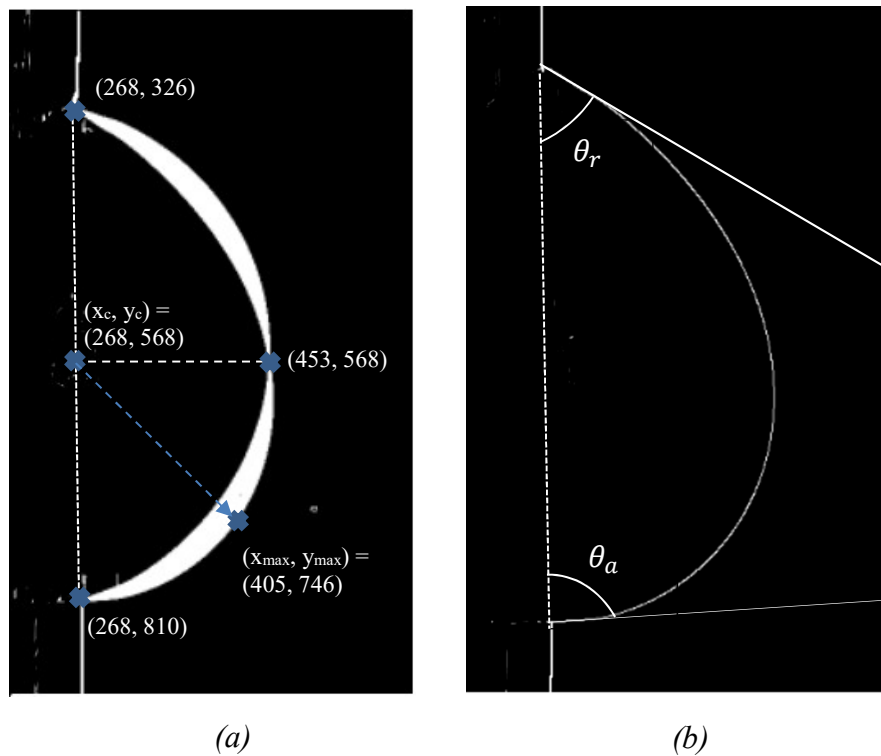
Figure 22. *(a)* **100 superimposed drop outlines with pixel coordinates for all nodes, droplet center and point of maximum distance from droplet center** *(b)* **outline passing through (x_{max}, y_{max}) with advancing and receding angles**

40

The contact angle hysteresis (CAH) was then found by subtracting the receding contact angle from the advancing contact angle as given by Equation 18.

$$\Delta\theta = \theta_a - \theta_r \qquad (18)$$

After using the Celestini's equation [61] to estimate the true corresponding resonance frequency within a range of ± 5 Hz, the search for the actual resonance frequency was undertaken by setting the search steps to ± 1 Hz and then to ± 0.5 Hz. Resonance frequencies were found for all the droplet-surface combinations in the same manner. During the identification process the acceleration of the surface was kept to a constant and low value to avoid droplet sliding. Details on how the resonance frequency was determined using the experimental system and software can be found in the flowcharts given in Figures 24 and 25.
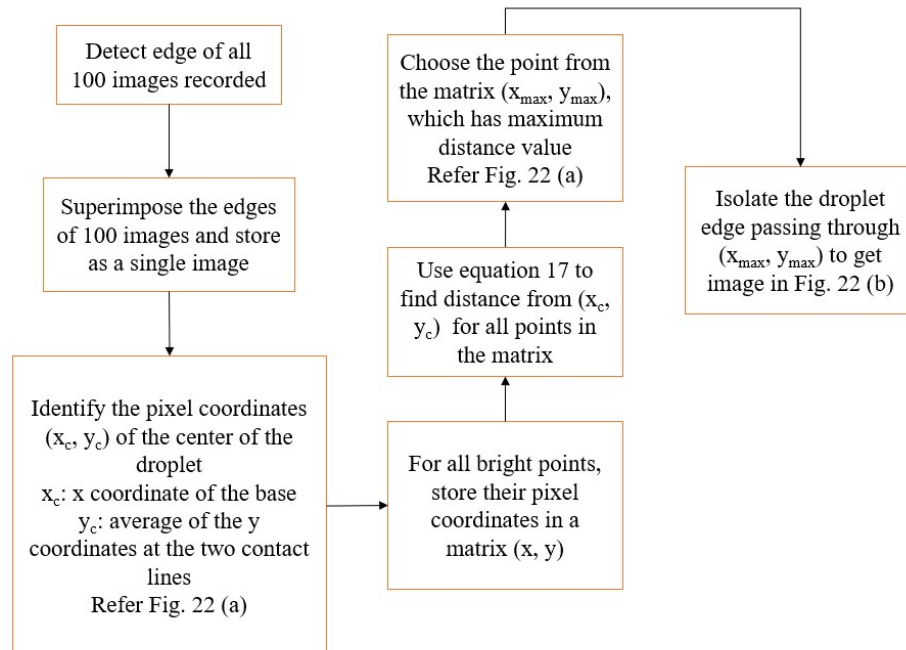
Figure 23. Procedure for extracting the maximum deflection droplet outline
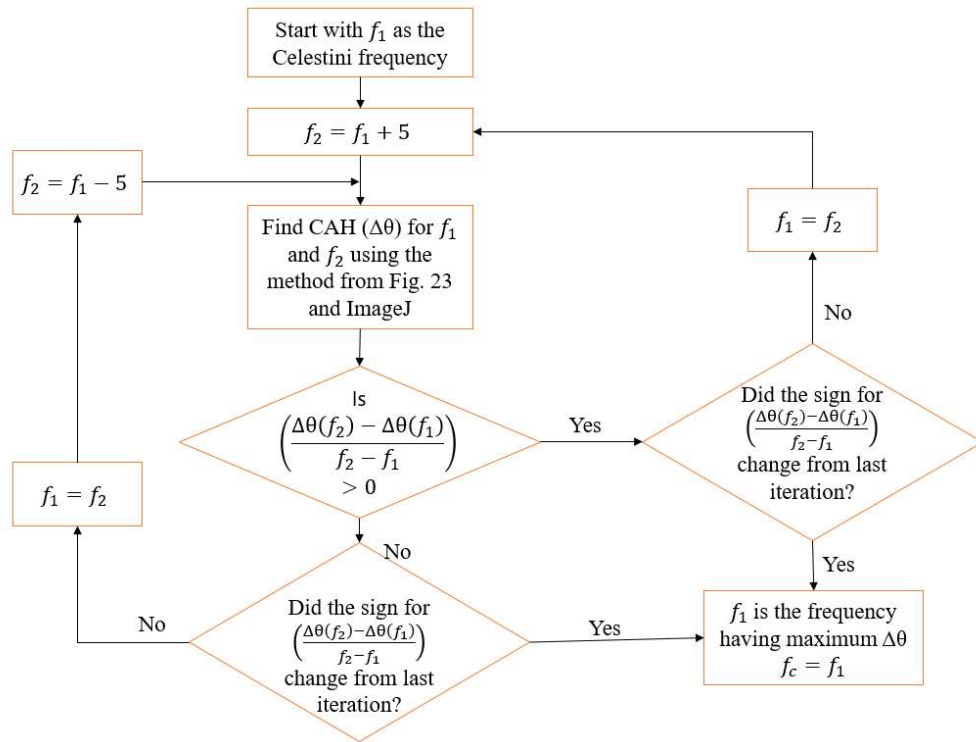
Figure 24. Procedure for resonance frequency search with a step size of 5 Hz
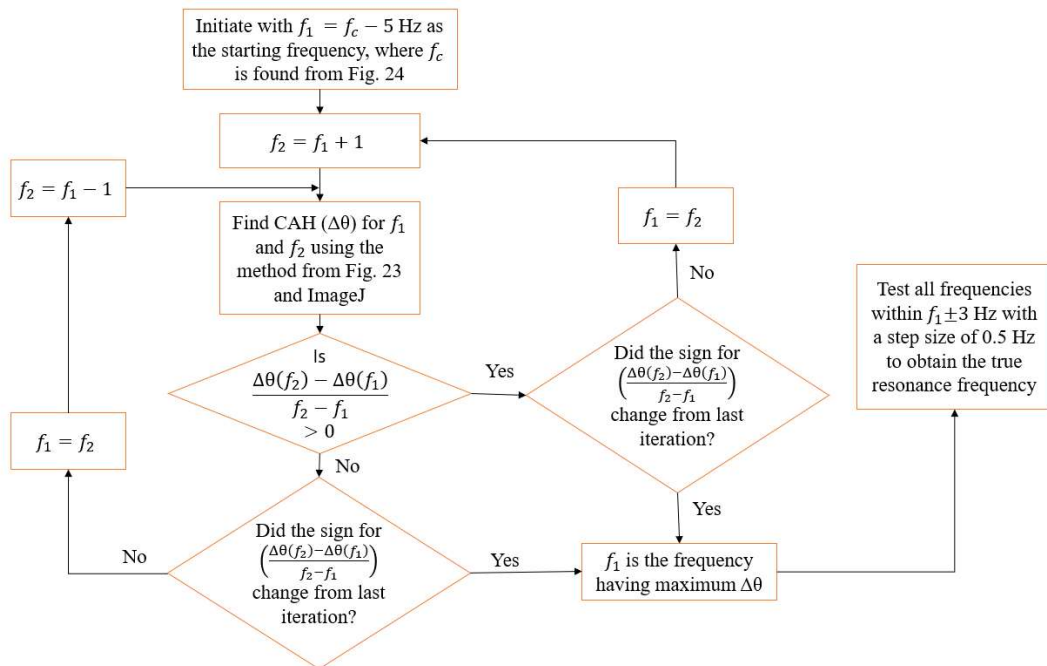
Figure 25. Procedure for resonance frequency search with a step size of 1Hz and 0.5 Hz

42

3.2.3 Identification of sliding threshold amplitude of droplets on different substrates

For each droplet volume – surface combination, the surface was vibrated at the identified resonance frequency starting from low amplitudes (accelerations). The acceleration was gradually increased until the droplet started to slide. Droplet sliding was identified when there was a shift in at least one of the two droplet contact lines as shown in Fig. 26. Details on how the sliding amplitude (acceleration) was determined using the experimental system and software can be found in the flowchart given in Fig. 27

The same experiment was repeated for all the droplet-surface combinations. Moreover, each experiment was repeated at ± 4 Hz and ± 8 Hz of the resonance frequency for each droplet-surface combination to determine the required threshold amplitudes for droplet sliding. Comparisons among all the droplet sliding threshold amplitudes are included and discussed in the results chapter of this thesis

(a)   *(b)*
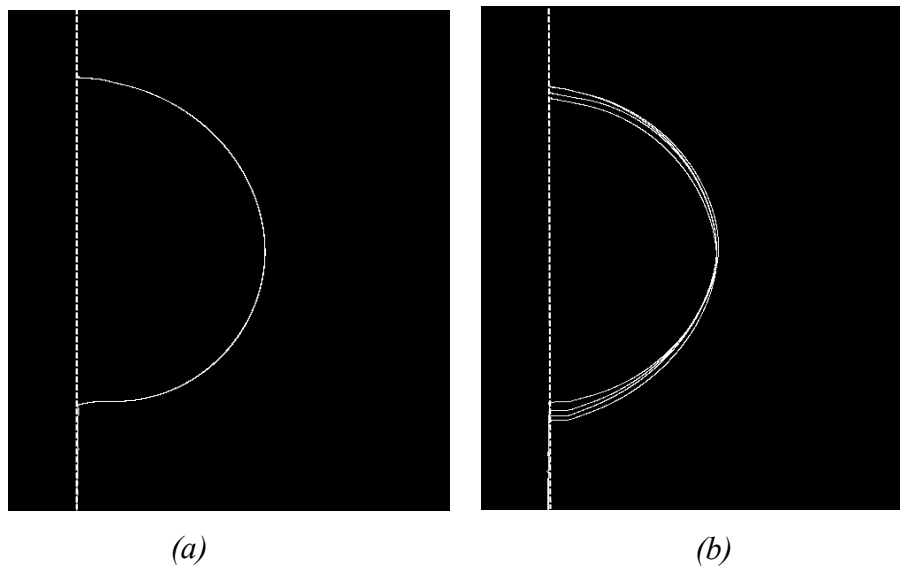
Figure 26. *(a)* Droplet pinned to the surface *(b)* droplet sliding on the surface
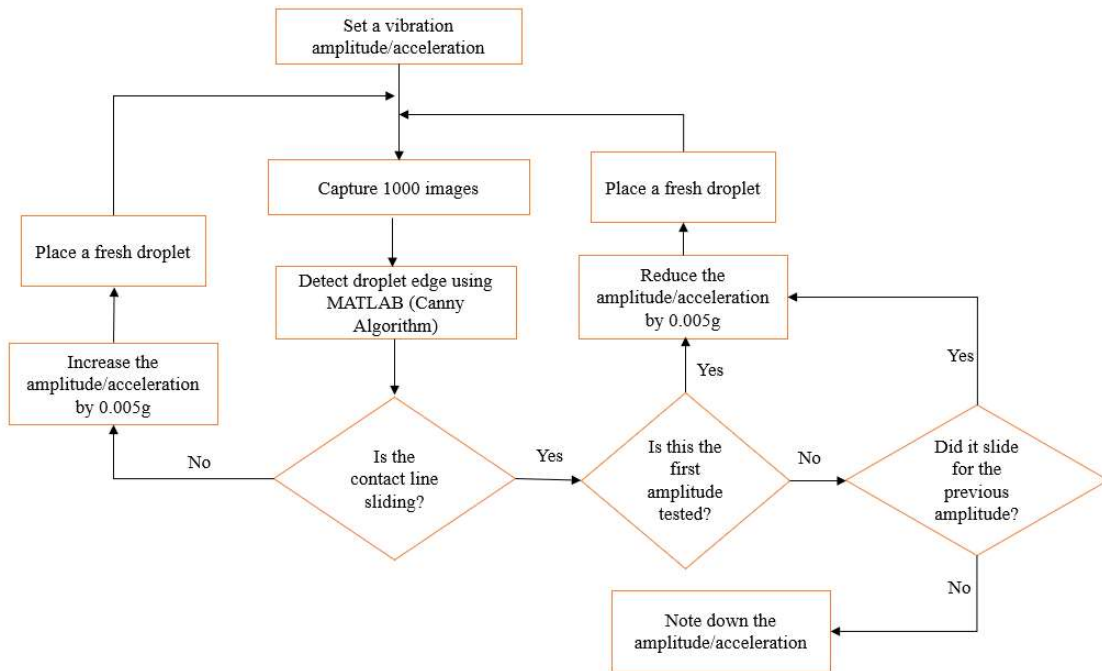
Figure 27. Procedure for identifying droplet sliding amplitude for a single droplet volume - surface combination

3.3 Experimental setup for condensation experiments

To study the effects of the vibration frequencies and amplitudes found in previous sections on drop wise condensation (DWC), a condensation chamber was built as shown in Figures 28 and 29. The entire set up was placed on top of a pneumatically damped optical table to reduce noise from ambient sources. Description of each system component can be found below.
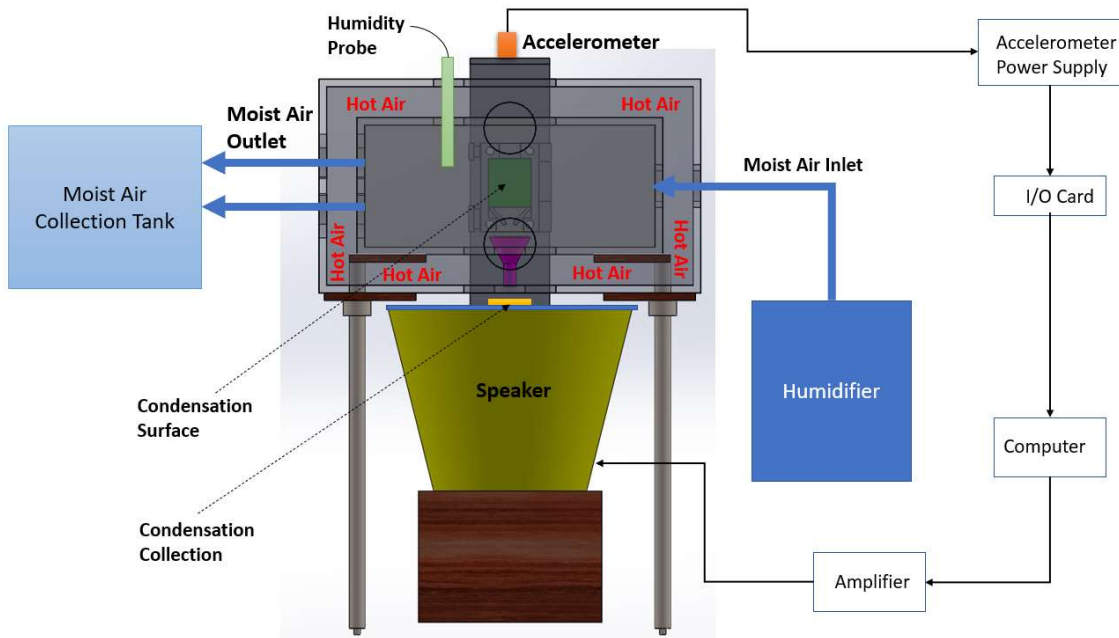
Figure 28. Condensation setup (front view)
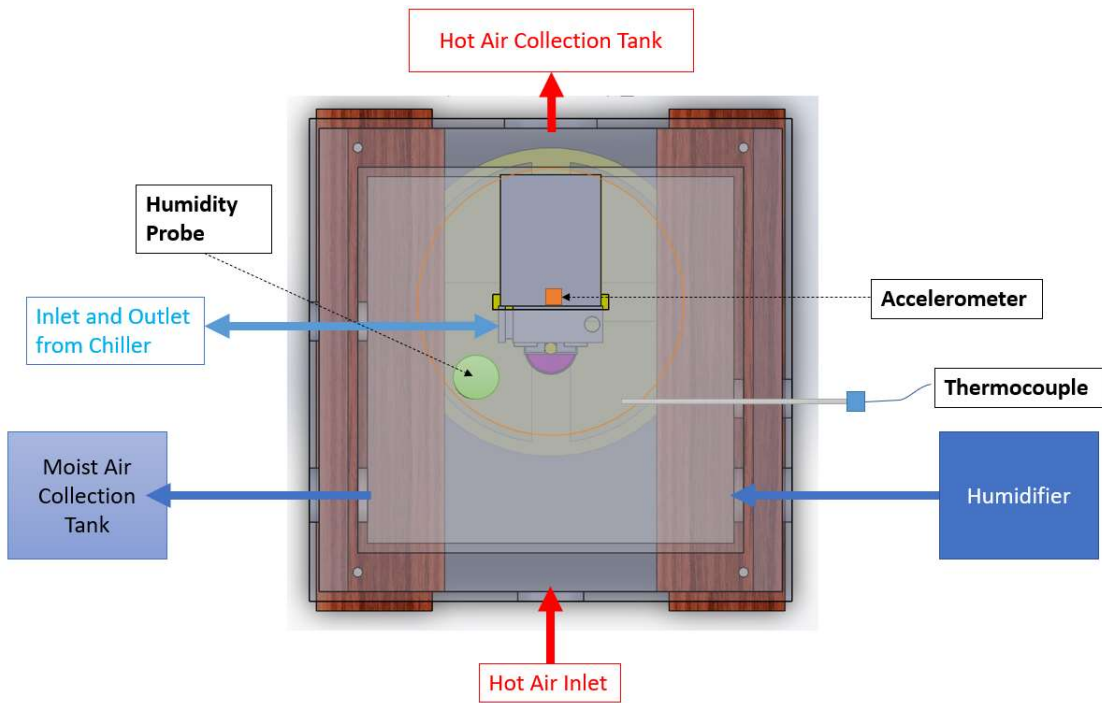
Figure 29. Condensation setup (top view)

3.3.1 Condensation surface - cold plate - chiller system

The condensation surface was attached to a 40 mm by 40 mm aluminum cold plate through an intermediate copper plate as shown in Fig. 30. Thermal grease was applied between the condensing surface and the copper plate, while thermal epoxy was used to attach the copper plate with the cold plate. A chiller (Thermo Neslab Merlin M25 Circulating Chiller) as shown in Fig. 31 was connected to the cold plate to provide chilled water to cool the surface. The insulated chiller lines were connected to the cold plate through the inlet and outlet holes provided in inner and the outer chambers, as shown in Fig. 29.

(a)

□ Aluminum Cold Plate
■ Copper Plate
■ Condensation Surface
■ Insulation
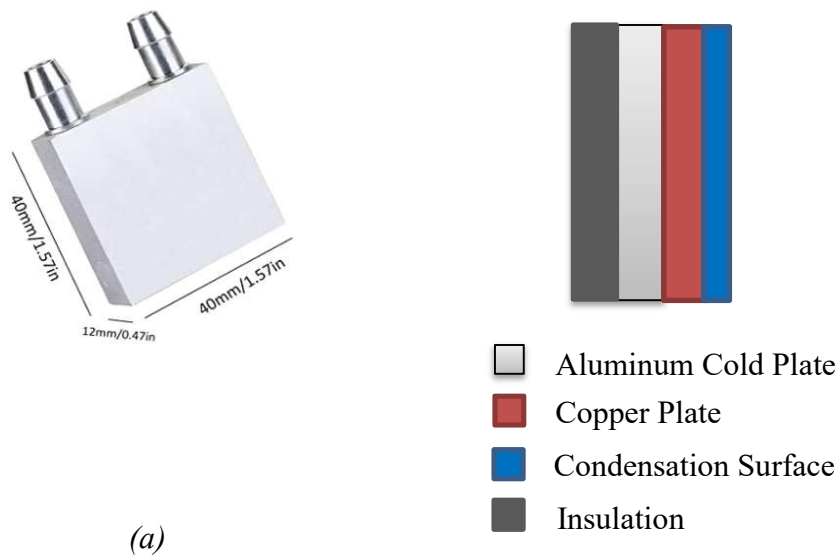
Figure 30. *(a)* **40 mm by 40 mm aluminum cold plate** *(b)* **cold plate – condensation surface assembly**

(b)

Figure 31. Thermo NesLab M25 Merlin Circulating Chiller

3.3.2 Cold plate vibration system

A stand as shown in Fig. 32 was fabricated to mount the cold plate – condensing surface assembly. 3D printed mounts were made to sandwich the cold plate and condensing surface and were securely bolted to the stand using plastic screws as shown in Fig. 32. The stand was attached to the woofer of the speaker in a manner similar to the setup used in the droplet wetting experiments. A sound speaker (1070 Infinity Reference, Infinity Inc.) as shown in Fig. 33 was connected to an amplifier (Russound P75-2 Channel Dual Source 75 W), which was used to provide lateral vibrations to the cold plate. The sound speaker provided optimal vibration response as described in the appendix. Vibration frequencies were provided using the Online tone generator [76].

(a)   *(b)*
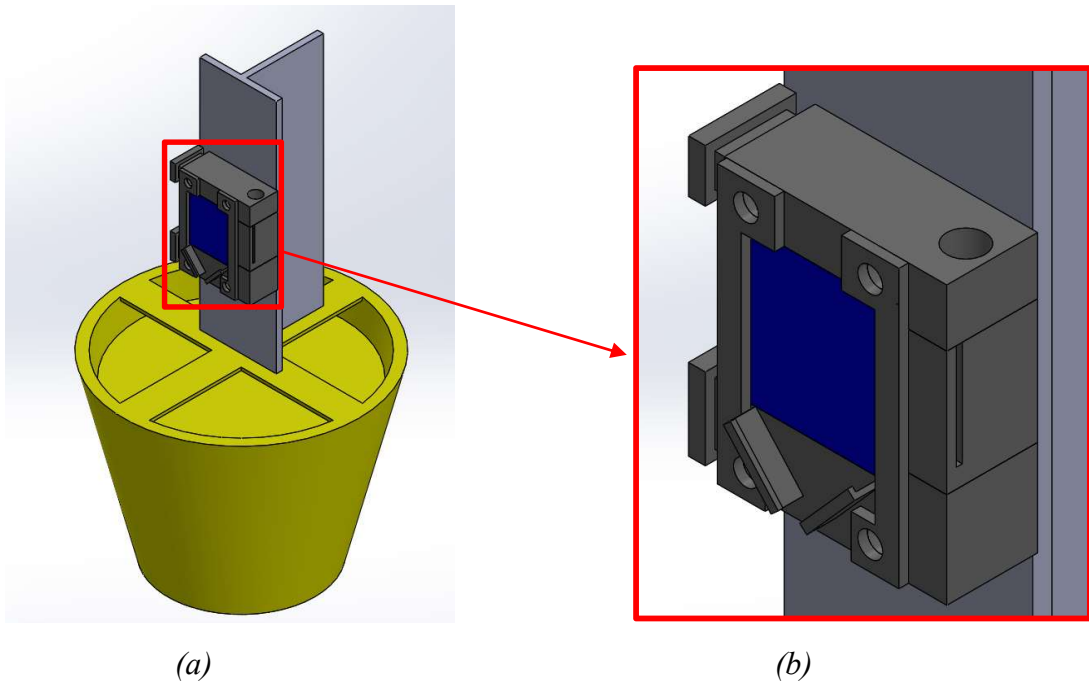
Figure 32. (a) Cold plate mounting stand (b) 3D printed surface holders (in dark grey)

Figure 33. 1070 reference subwoofers, Infinity Inc.

3.3.3 Condensation chamber

Two chambers (inner and outer) both made from cast acrylic (sheets from McMaster-Carr) were designed and fabricated as shown in Fig. 28. The inner chamber was 25.4 cm × 25.4 cm × 11.43 cm while the outer chamber was 31.75 cm × 31.75 cm × 17.78 cm, in dimensions. Detailed drawings of the inner and outer chamber walls as well as the cold plate stand are given in the appendix.

The inner chamber received the moist air and housed the cold plate-condensing surface assembly. The moist air was generated by a humidifier (LV600HH, Levoit) as shown in Fig. 34. The humidifier was equipped with three mist and heat level settings. A mesh was kept between the inlet and outlet, and the cold surface to avoid convection current or flow effects. The space between the inner and outer chambers was heated using hot air to avoid condensation on the walls of the inner chamber. Hot air at 65 °C was provided by a hot air gun (FURNO 500, Wagner SprayTech) as shown in Fig. 35. The moist air entered the inner chamber through a single inlet and exited through two outlets to minimize turbulence within the inner chamber. Moreover, the moist air exited through the two outlets without mixing with the hot air. The hot air entered via a single inlet and exited via two outlets, only through the outer chamber.

A V-shaped open channel (i.e., liquid gutter) was placed at the bottom of the surface holder to direct the flow of condensate to condensation collection point as shown in Fig. 32(b). A funnel was attached just below the V-extrusion on the bottom wall of the inner chamber to collect the condensate. All precautions were taken to ensure that the condensate collected only came from the condensation surface.

Figure 34. Humidifier, LV600HH, Levoit

Figure 35. Hot Air Gun, FURNO 500 Wagner SprayTech

3.3.4 Instrumentation

Two T-type bead thermocouples were attached to the side of the condensing surface to measure surface temperatures. One T-type probe thermocouple was inserted in the inner chamber to measure bulk air temperature. A temperature-humidity probe (ERAY) was used to keep track of humidity and temperature inside the chamber as shown in Fig. 36. The temperature-humidity probe can measure temperatures from -30 °C - 60

°C with an accuracy of ± 0.5 °C and measure humidity ranging from 0 – 100 % with an accuracy of ± 3%. Furthermore, it has a fast response time of 10 s and a resolution of 0.01 for both temperature and humidity. All the instrumentation apart from the humidity probe was attached to a data acquisition system (Agilent 34970A) as shown in Fig. 37. An accelerometer (352C04, PCB Piezoelectronics) was connected on top of the stand as shown in Fig. 28, to measure the acceleration of the system under vibrations. The accelerometer was connected to an accelerometer power supply (P5000, MISTRAS) and then to the I/O card (NI USB-5132), like the vibration setup used in the wetting experiments.

Figure 36. Temperature - Humidity Probe, ERAY

Figure 37. Agilent 34970A

3.4 Methodology for condensation experiments

The experiment was started by turning on the hot air gun, to let the walls of the inner chamber heat up. The pre-heat from the hot air gun was continued for 10 minutes on the lowest setting of the gun (65 °C). Then, the chiller was turned on and set to a temperature of 12 °C. Lastly, the humidifier was turned on to let moist air into the chamber. The humidifier was kept at the lowest mist level and non-heating mode. The system reached steady state in approximately one hour and steady state was identified by keeping track of surface and moist air temperatures and relative humidity.

Once steady conditions were achieved in the condensation chamber, condensate was collected for the without-vibration case for 30 minutes. Then, the vibration system was turned on and set to the required frequencies and amplitudes. Initially the identified resonance frequency for the smallest volume was used for both resonance and sliding experiments. The amplitude/acceleration of vibration imposed was 20% higher than the sliding threshold amplitude found for the corresponding droplet volume. Condensate was

52

collected for 30 minutes when vibrations were applied. For the final two tests, a frequency sweep from 50 – 70 Hz and 70 – 50 Hz with the amplitude being controlled within a specific range were conducted. These two tests were also conducted for the same time interval as in the first two cases (i.e., for 30 minutes). The system was kept running for thirty (30) minutes without vibrations and in between any two vibration tests to block or diminish the long-term (history) effects of vibrations. After each test, the mass of the condensate was measured using a micro-balance (APEX Series, Denver Instrument). These tests were done using Copper 110 and PTFE as condensation surfaces.

.

CHAPTER IV

RESULTS AND DISCUSSION

Five surfaces having static contact angle with DI water ranging from 70º - 110º were chosen for the droplet wetting experiments. Static contact angle with DI water droplets was initially determined on all the surfaces. The droplets were dispensed using a micro-pipette, which was calibrated beforehand. The micro-pipette calibration and static contact angle results are presented in the first two sections. Resonance frequencies for droplets ranging from 3 – 5 µL, were experimentally identified on the five surfaces are then presented and discussed. In the next section, results pertaining to the droplet sliding threshold amplitudes/accelerations are presented and discussed as well. Finally, in the last section, results obtained from condensation tests on copper and PTFE are presented.

4.1 Micro-pipette calibration

Micro-liter droplets were placed on the surfaces with the help of a micro-pipette designed to dispense droplets having volumes ranging from 0.5 – 10 µL. The micro-pipette was calibrated before using it in the droplet wetting experiments. A droplet corresponding to a volume on the micro-pipette (uncorrected volume) was dispensed on a micro-balance (APEX Series, Denver Instrument) to measure the mass of the droplet. The process was repeated for a total of five times for a single uncorrected volume and the average mass was used for calculation purposes. Mass of six different uncorrected volumes was measured following the procedure explained above. The mass was then converted to volume using the density of water of 0.997 mg/µL. The results of the calibration process are presented in Table 2 and Fig. 38.

Table 1. Micro-pipette calibration

Uncorrected Volume(µL)	Mass (milligrams)	Average Mass (milligrams)	Actual Volume (µL)
2.5	2.6	2.48	2.49
	2.4		
	2.4		
	2.4		
	2.6		
3	3.0	2.98	2.99
	3.0		
	3.1		
	2.9		
	2.9		
3.5	3.6	3.52	3.53
	3.5		
	3.3		
	3.8		
	3.4		
4	3.8	3.98	3.99
	4.0		
	4.1		
	3.9		
	4.1		
4.5	4.4	4.48	4.49
	4.4		
	4.6		
	4.5		
	4.5		
5	5.2	4.94	4.95
	4.9		
	4.9		
	4.8		
	4.9		

Figure 38. Micro-pipette calibration curve

The calibration equation for the micro-pipette readings is given by Equation 19. The R^2 value for the calibration equation was 0.9994, which indicated a strong linear relation between the micro-pipette volume setting and the actual volume of the dispensed droplet.

$$Actual\ Volume = (0.9893 \times Uncorrected\ Volume\ ) + 0.0315 \qquad (19)$$

4.2 Static contact angle determination on different surfaces

Each droplet was dispensed and place on each surface horizontally. Left and right contact angles were determined following the procedure outlined in Chapter 3. Static contact angle (SCA) was calculated by taking the average between the left and right

contact angles. For each surface, SCA were found for four droplet volumes ranging from 3 – 5 µL. The grand average of all four SCA was taken as the final static contact angle. Furthermore, the standard deviation in the four SCA was also determined. Table 2 shows the static contact angle data and volumes tested for all surfaces.

Table 2. Static contact angle for droplet volume - surface combinations. Reprinted with permission from [68]

Substrate	Static Contact Angle (º)	Calibrated Droplet Volumes Tested (µL)
Al 6061	74.2 ± 1.80	3.30, 3.79, 4.29, 4.78
Cu 110	85.5 ± 1.30	3.30, 3.79, 4.29, 4.78
Polystyrene	93.0 ± 1.06	3.30, 3.79, 4.29, 4.78
PTFE	100.6 ± 0.7	3.30, 3.79, 4.29, 4.78
Wax	105.0 ± 0.6	3.30, 3.79, 4.29, 4.78

4.3 Characterization of surface-vibration system

Before conducting droplet wetting experiments under the effects of vibration, the experimental system was vibrated at a different, single frequencies to evaluate its response to the input vibration parameters provided by the Online tone generator. To test the frequency response of the system, vibration experiments were performed on the system before initiating the resonance frequency identification experiments. The system was vibrated at frequencies ranging from 35 to 85 Hz to ascertain a good and clean frequency response of the system. Fast Fourier Transform (FFT) results for two of the frequencies

are shown in Fig. 39, which show a clean frequency response without interference from other potential vibration modes. In summary, the lab set up designed and built for the experiments behaved as expected and produced no higher-order harmonic effects.
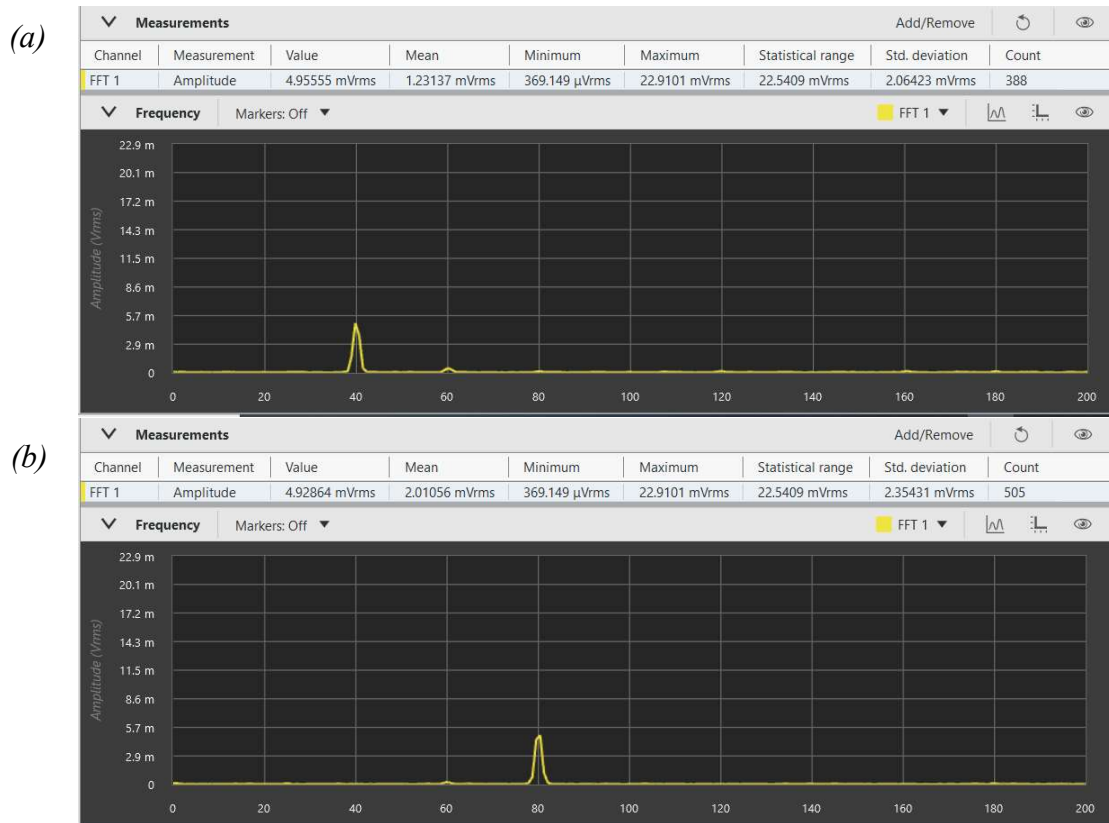
Figure 39. FFT for an imposed frequency on the system at *(a)* 40Hz *(b)* 80 Hz at 0.05g

4.3 Experimental identification of resonance frequency for droplet volume-surface combinations

As discussed in depth in the previous chapter, the resonance frequency was identified as the frequency at which the droplet had the largest contact angle hysteresis. During the identification process the acceleration for each surface was kept at a low

constant value for all droplet volumes to avoid droplet sliding. Resonance frequencies were identified for each droplet volume-surface combination as shown in Table 2. Contact angle hysteresis (Δθ) as a function of imposed frequency for different surfaces are shown in Figures 40 to 43
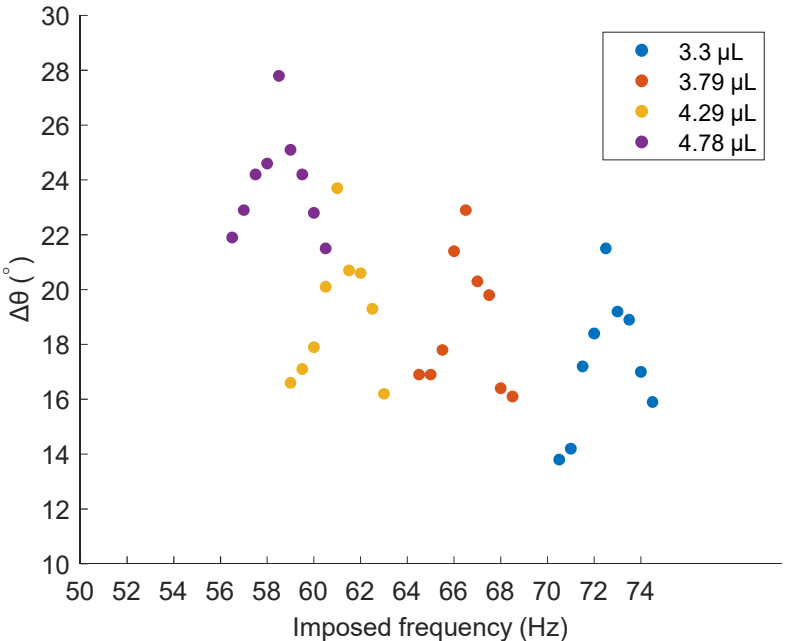
Figure 40. Contact angle hysteresis as a function of imposed frequency using aluminum 6061 as substrate
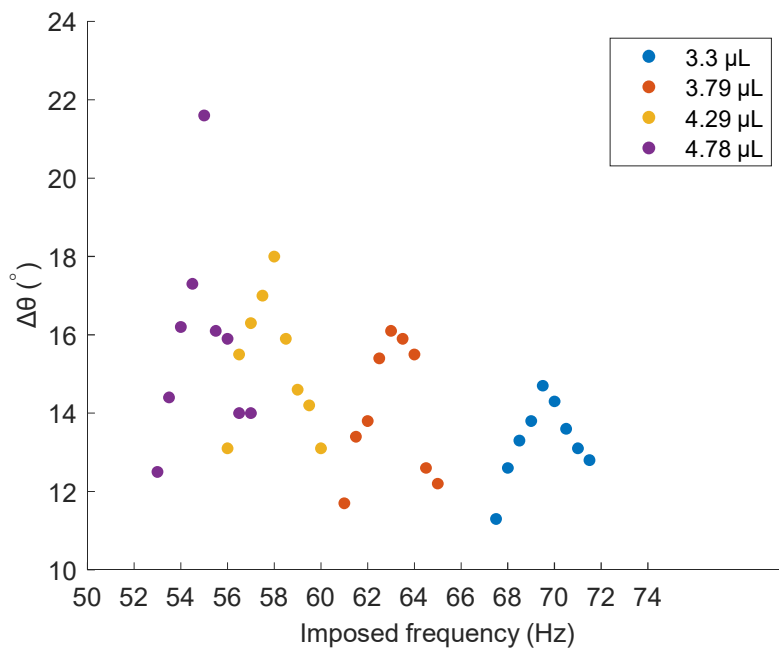
Figure 41. Contact angle hysteresis as a function of imposed frequency using copper 110 as substrate
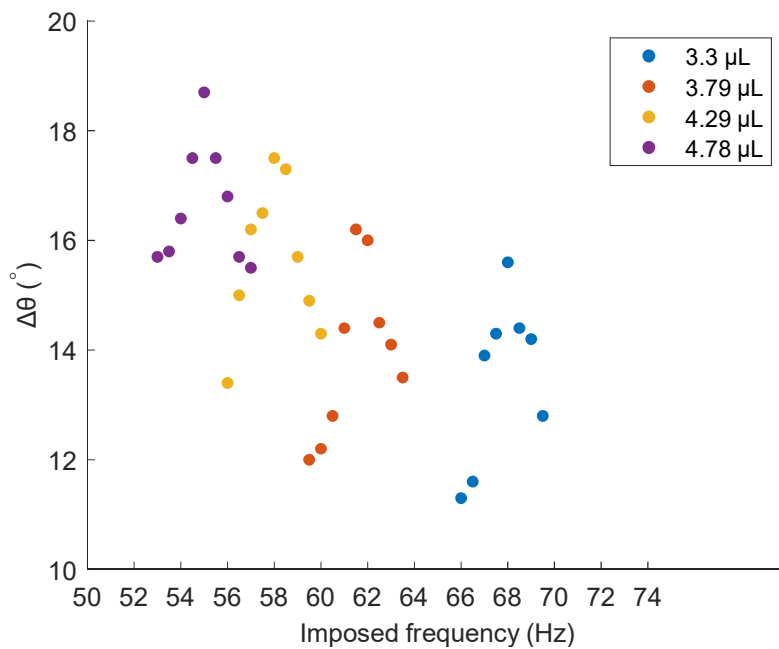
Figure 42. Contact angle hysteresis as a function of imposed frequency using polystyrene as substrate
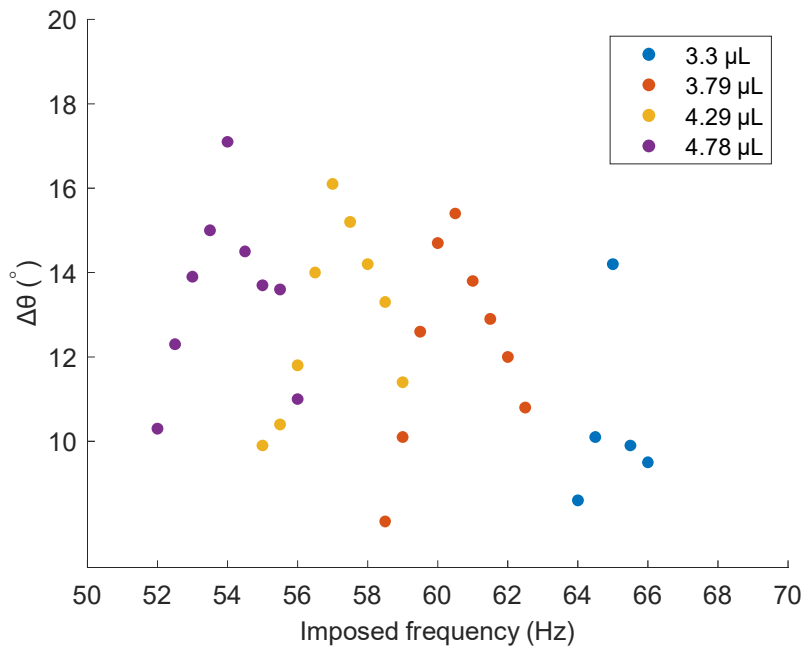
Figure 43. Contact angle hysteresis as a function of imposed frequency using PTFE as substrate

From Figures 40 – 43, it can be seen that the contact angle hysteresis for each droplet volume reaches a maximum at a certain imposed frequency. The frequency at which the maximum contact angle hysteresis is reached, is identified to be the first mode (rocking mode) resonance frequency for the droplet.

For each surface, the resonance frequency decreases with increasing droplet volume. Furthermore, for each droplet volume, resonance frequencies decrease with increasing static contact angle. These results agree with well-established numerical and experimental models developed to predict resonance frequency of droplets [61-63, 80], which give an inverse relationship between the resonance frequency and both, the radius of the droplet and the static contact angle of the droplet with the surface. Furthermore, for

61

a given low value of acceleration, larger droplets show a greater contact angle hysteresis as explained by Celestini *et al.* [61]. Resonant frequencies for all the droplet-surface combinations can be found in Table 3.

To obtain the resonance frequencies as a function of static contact angle, the resonance frequencies were normalized with droplet volume by using Equation 20.

$$f_{normalized} = \frac{2\pi f}{\left(\frac{\gamma}{\rho R^3}\right)^{0.5}} \tag{20}$$

where, $R = \left(\frac{3V}{\pi(1-cos\theta_e)^2(2+cos\theta_e)}\right)^{1/3}$

R is the radius at the belly of the droplet, while γ, ρ and f are the surface tension of water (0.072 N/m), density of water $\left(997 \frac{kg}{m^3}\right)$ and the resonant frequency for the droplet with radius R. Experimentally obtained resonance frequencies for all volume-surface combinations as well as the corresponding normalized frequency and acceleration ratio (a/g) are shown in Table 3.

Table 3. Experimentally identified resonance frequencies for all droplet volume-surface combinations. Reprinted with permission from [68]

Surface	SCA (°)	SCA Standard Deviation (°)	Droplet Volume (µL)	$\frac{a}{g}$ imposed	Resonance Frequency (Hz)	$f_{normalized}$ (-)
Al 6061	74.2	1.8	3.3	0.020	72.5	2.73
			3.79		66.5	2.68
			4.29		61	2.62
			4.78		58.5	2.65
Copper 110	85.5	1.3	3.3	0.025	69.5	2.16
			3.79		63	2.1
			4.29		58	2.05
			4.78		55	2.06
Polystyrene	93.0	0.9	3.3	0.025	68	1.91
			3.79		61.5	1.85
			4.29		58	1.86
			4.78		55	1.86
PTFE	100.6	0.7	3.3	0.011	65	1.682
			3.79		60.5	1.677
			4.29		57	1.681
			4.78		54	1.681

Simulations were performed for drops supported on vertical planar surfaces undergoing lateral vibrations by Sakakeeny *et al.* [68]. In the simulations, the authors considered static contact angles in the range from 40° - 160° and proposed an analytical expression to determine the resonance frequency of the droplets as a function of static contact angle and Bond number.

The experimentally obtained normalized frequencies and the normalized frequencies obtained through simulations for the experimental test cases are plotted as a

function on contact angle as shown in Fig. 44. The horizontal error bars in Fig. 44 represent the standard deviation values in static contact angles. The uncertainty in normalized frequency (i.e., the lower and upper limits) was found using Equation 20 with static contact angles as $\theta_{upper} = \theta_e + \sigma_{\theta_e}$ and $\theta_{lower} = \theta_e - \sigma_{\theta_e}$ respectively, where σ_{θ_e} is the standard deviation in SCA. As seen from Fig. 44, there is a good agreement between the experimental and the simulation results, which helps to validate the model by proposed Sakakeeny *et al.* [68].
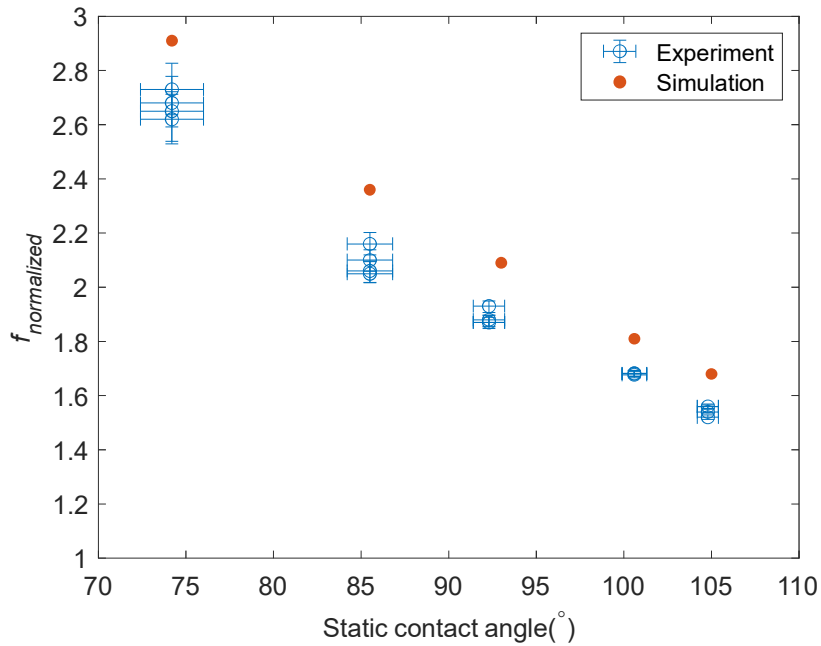
Figure 44. Comparison between normalized frequencies from the current experiments and simulations [68] as a function of static contact angle

As Figure 44 shows, the model slightly over-predicts the experimental data, which is discussed at length in the publication [68]. However, the discrepancy for all cases was less than 12%, which is less when compared to other models [61, 63, 80].
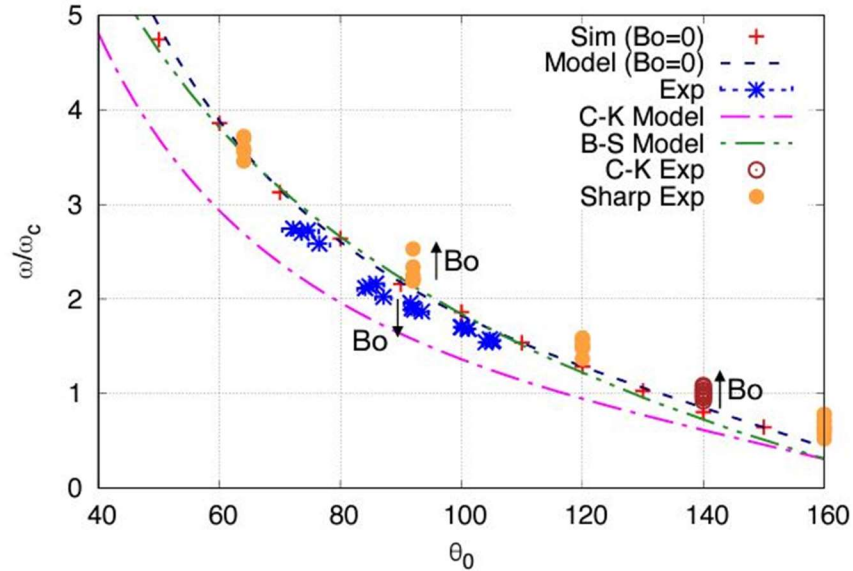
Figure 45. Comparison between the present experimental data and similar numerical and experimental studies. Reprinted with permission from [68]

Figure 45 shows the comparison between the normalized resonance frequency obtained experimentally and the normalized resonance frequency derived using different models and the simulation results obtained by Sakakeeny *et al.* [68]. It can be seen that the current experimental data agree well with the numerical simulation data and model developed by Sakakeeny *et al.* [68] (simulation and model at Bond number of 0.0), which closely follows the model developed by Bostwick *et al.* [80]. The latter does not consider the effect of Bond number, which could be a possible reason for the larger discrepancy. Furthermore, for the experiments conducted by Sharp *et al.* [63], the normalized frequency tends to increase with Bond number while for the present experiment show an opposite trend [68]. The experiments by Sharp *et al.* [63] were conducted on a horizontal surface under longitudinal vibrations where this trend is expected [67]. In the current study,

experiments were conducted by placing droplets placed on a vertical surface, which could explain the difference between both data sets.

Table 4 shows the comparison between resonance frequencies calculated from Celestini's model using Equation 13 and the resonance frequencies obtained experimentally. In Fig. 46, the normalized resonance frequencies obtained experimentally, and the normalized resonance frequencies calculated using the Celestini's equation are plotted as a function of static contact angle. The resonance frequencies calculated from Celestini's equation were normalized in the same manner as the experimentally obtained resonance frequencies by using Equation 20.

Table 4. Comparison of experimental resonance frequencies with resonance frequencies calculated using Celestini's model

Surface	SCA (º)	Droplet Volume (μL)	Experimental Resonance Frequency (Hz)	Model Resonance Frequency (Hz)	% Difference
Al	74.2	3.3	72.5	61.9	17%
		3.79	66.5	57.7	15%
		4.29	61	54.2	13%
		4.78	58.5	51.4	14%
Cu	85.5	3.3	69.5	59.8	16%
		3.79	63	55.8	13%
		4.29	58	52.4	11%
		4.78	55	49.7	11%
PS	92.3	3.3	68	57.3	19%
		3.79	61.5	53.4	15%
		4.29	58	50.2	16%
		4.78	55	47.6	16%
PTFE	100.6	3.3	65	53.9	21%
		3.79	60.5	50.3	20%
		4.29	57	47.3	21%
		4.78	54	44.8	21%
Wax	104.8	3.3	62	51.6	20%
		3.79	57	48.2	18%
		4.29	55	45.3	21%
		4.78	52	42.9	21%
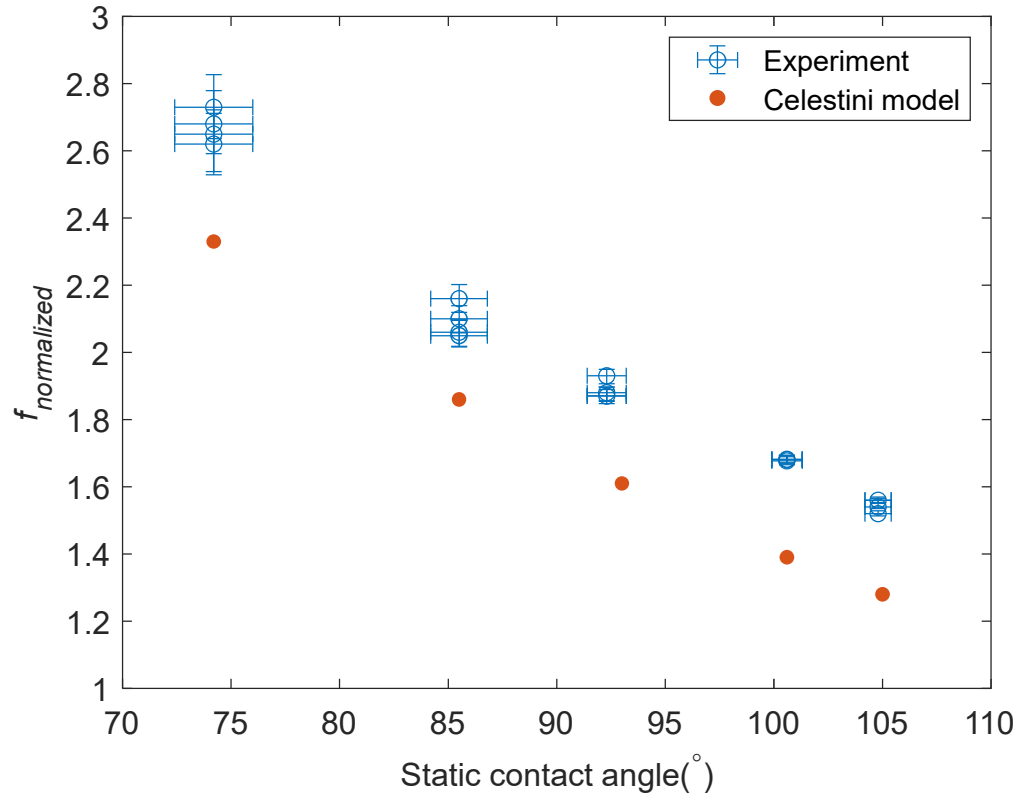
Figure 46. Comparison between normalized experimental and Celestini's model-based frequencies

As seen from Table 4 and Fig. 46, Celestini's equation underpredicts the true experimental resonance frequency up to a maximum of 21% difference with an average relative difference of 17.3%. It is worth noting that the Celestini's model does not consider the kinetic energy of the fluid motion inside the droplet during vibration, which could be a potential cause for the underpredicted resonance frequency values [68]. Furthermore, the normalized frequency for a single static contact angle (or surface) varies with drop volume or the Bond number of the droplet. However, this is not the case for the normalized frequency calculated by using the Celestini model. This could be because the Celestini

model was developed for droplets on horizontal surfaces and does not consider the effect of Bond number [61].

4.4 Effect of resonant vibrations on droplet mobility for droplet volume-surface combinations

One of the objectives of the study was to study the effect of vibrations on droplet sliding at resonance frequencies and in the close vicinity of resonance frequencies. As discussed in the previous chapter, for each frequency imposed, the acceleration of the substrate was kept at a low value and gradually increased to identify the threshold amplitude at which droplet sliding occurred. The substrate acceleration at which sliding occurred was measured using the accelerometer as a root mean square (RMS) value. This value was used to calculate the RMS amplitude and vibration intensity required, as given by Equations 21 and 22.

$$A = \frac{a}{(2\pi f)^2} \tag{21}$$

$$I = A \times (2\pi f) = \frac{a}{(2\pi f)} \tag{22}$$

From the above equations, it is evident that the amplitude and vibration intensity for a fixed frequency are directly related to the acceleration. Therefore, the amplitude and vibration intensity should depict the same trend as acceleration. The sliding threshold acceleration values as a function of imposed frequency, for different droplet volume-surface combinations are shown in Figures 47 to 50. For simplicity purposes, the acceleration has been normalized with respect to g (9.81 m/s^2) and the corresponding

acceleration ratio (*a*/*g*) value is shown as a function of imposed frequency. Furthermore, the *a*/*g* values and the corresponding amplitudes and vibration intensities for each droplet-surface combination are shown in Tables 5 to 8.
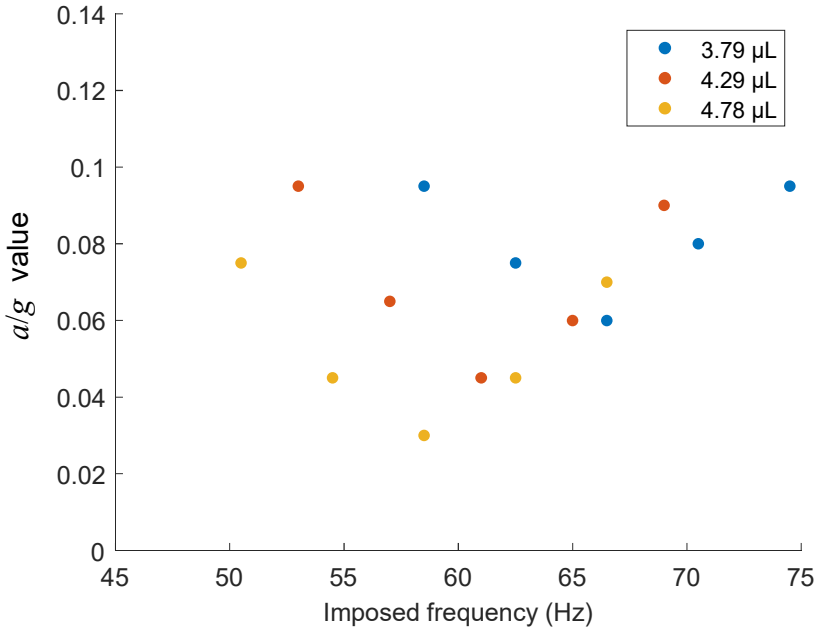
Figure 47. Droplet sliding threshold acceleration as function of imposed frequency using aluminum 6061 as substrate
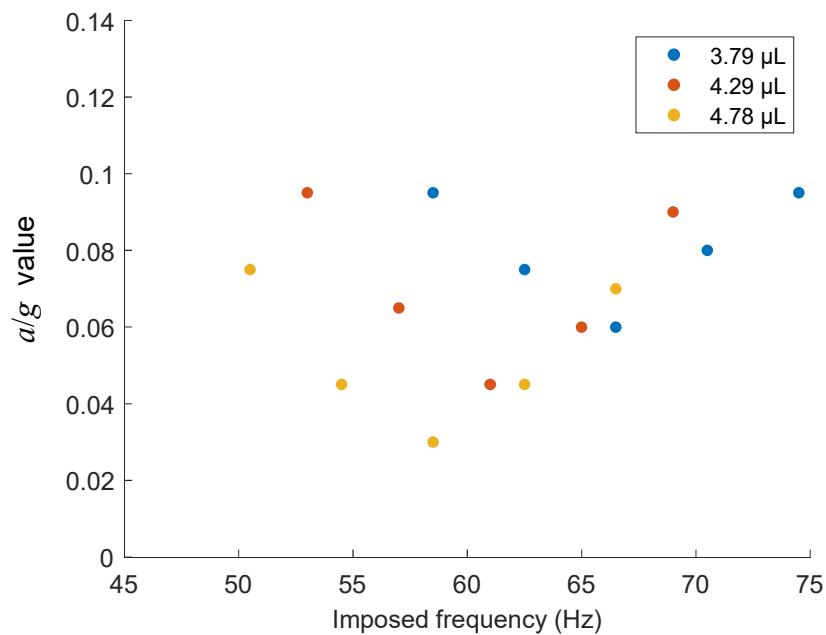
Figure 48. Droplet sliding threshold acceleration as function of imposed frequency using copper 110 as substrate
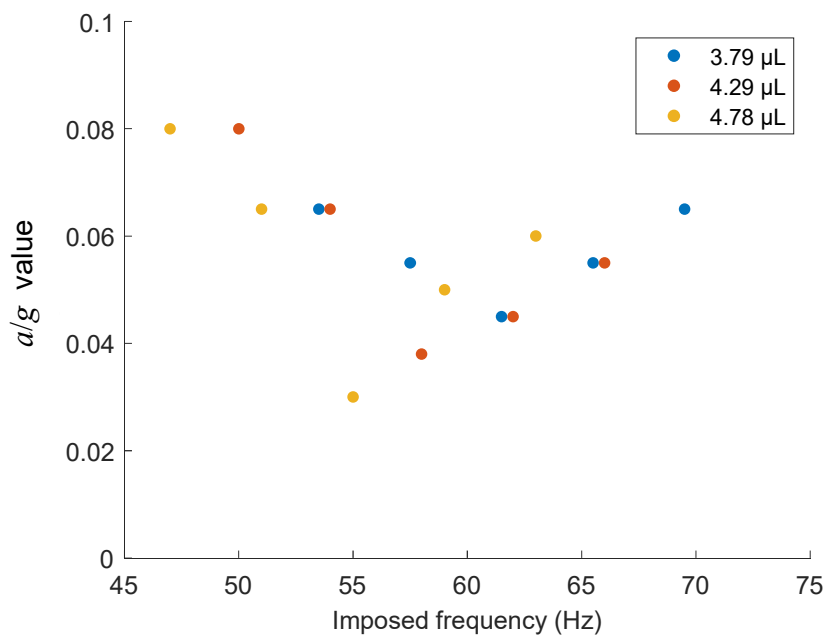
Figure 49. Droplet sliding threshold acceleration as function of imposed frequency using polystyrene as substrate
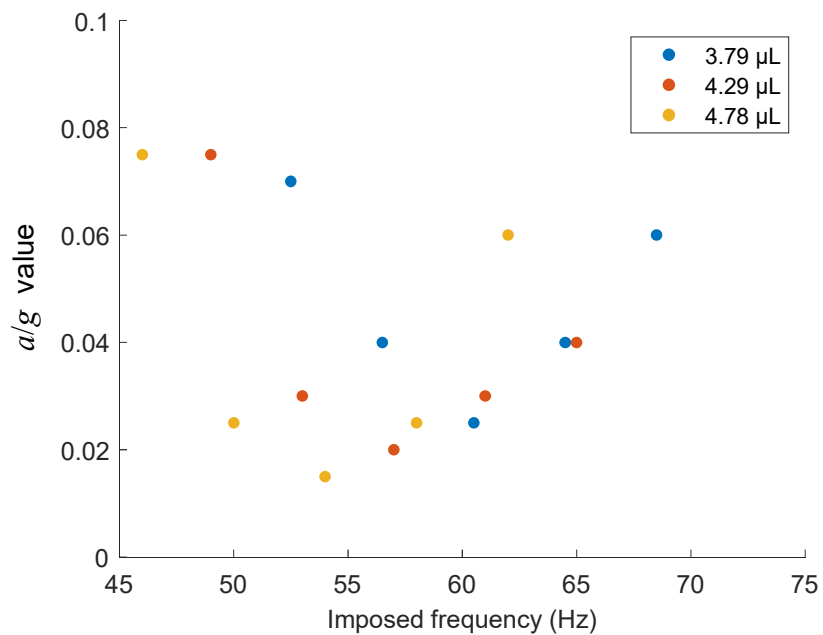
Figure 50. Droplet sliding threshold acceleration as function of imposed frequency using PTFE as substrate

Table 5. Droplet sliding results using aluminum 6061 as substrate

Drop Volume (μL)	Imposed Frequency (Hz)	$\frac{a}{g}$ value	Amplitude (μm)	Vibration Intensity (μm/s)
3.79	58.5	0.095	6.90	2536.2
	62.5	0.075	4.77	1873.2
	66.5*	0.06	3.37	1408.1
	70.5	0.08	4.00	1776.9
	74.5	0.095	4.25	1989.4
4.29	53	0.095	8.40	2797.3
	57	0.065	4.97	1780.0
	61*	0.045	3.01	1153.7
	65	0.06	3.53	1441.7
	69	0.09	4.70	2037.6
4.78	50.5	0.075	7.31	2319.5
	54.5	0.045	3.76	1287.6
	58.5*	0.03	2.18	801.3
	62.5	0.045	2.86	1123.1
	66.5	0.07	3.93	1642.1
* - Resonance frequency				

Table 6. Droplet sliding results using copper 110 as substrate

Drop Volume (μL)	Imposed Frequency (Hz)	$\frac{a}{g}$ value	Amplitude (μm)	Vibration Intensity (μm/s)
3.79	55	0.1	8.21	2838.8
	59	0.075	5.35	1984.7
	63*	0.05	3.13	1239.1
	67	0.08	4.43	1864.3
	71	0.11	5.42	2418.9
4.29	50	0.12	11.93	3747.1
	54	0.06	5.11	1734.8
	58*	0.04	2.95	1076.8
	62	0.07	4.53	1762.8
	66	0.1	5.70	2365.6
4.78	47	0.08	9.00	2657.6
	51	0.065	6.21	1989.9
	55*	0.03	2.46	851.6
	59	0.055	3.93	1455.5
	63	0.09	5.63	2230.4
* - Resonance frequency				

Table 7. Droplet sliding results using polystyrene as substrate

Droplet Volume (µL)	Imposed Frequency (Hz)	$\frac{a}{g}$ value	Amplitude (µm)	Vibration Intensity (µm/s)
3.79	53.5	0.065	5.64	1896.9
	57.5	0.055	4.13	1493.4
	61.5*	0.045	2.96	1142.4
	65.5	0.055	3.19	1311.0
	69.5	0.065	3.34	1460.2
4.29	50	0.08	7.95	2498.1
	54	0.065	5.54	1879.4
	58*	0.038	2.81	1022.9
	62	0.045	2.91	1133.2
	66	0.055	3.14	1301.1
4.78	47	0.08	9.00	2657.6
	51	0.065	6.21	1989.9
	55*	0.03	2.46	851.6
	59	0.05	3.57	1323.1
	63	0.06	3.76	1487.0
* - Resonance frequency				

Table 8. Droplet sliding results using PTFE as substrate

Droplet Volume (μL)	Imposed Frequency (Hz)	$\frac{a}{g}$ value	Amplitude (μm)	Vibration Intensity (μm/s)
3.79	52.5	0.07	6.31	2081.8
	56.5	0.04	3.11	1105.4
	60.5*	0.025	1.70	645.2
	64.5	0.04	2.39	968.3
	68.5	0.06	3.18	1367.6
4.29	49	0.075	7.76	2389.8
	53	0.03	2.65	883.8
	57*	0.02	1.53	547.8
	61	0.03	2.00	767.9
	65	0.04	2.35	960.8
4.78	46	0.075	8.81	2545.6
	50	0.025	2.49	780.7
	54*	0.015	1.28	433.7
	58	0.025	1.85	673.0
	62	0.06	3.88	1511.0
* - Resonance frequency				

From the above tables and figures, it can be seen that for each droplet volume – surface combination, when the imposed frequency is equal to the resonance frequency, the least amount of acceleration, amplitude and vibration intensities are required for droplet sliding. These results are in accordance with the results obtained by Boryeko and Chen [52]. They found that lowest vibration amplitudes are required for a Wenzel to Cassie transition at the first and second resonance modes for droplets on horizontally oriented on superhydrophobic surfaces. On similar lines, Daniel *et al.* [62] showed that the maximum

velocities for droplet motion on horizontal surfaces were achieved at the first and second resonance modes, which corroborate the results shown above.

Furthermore, the threshold acceleration required for droplet sliding reduces as the droplet volume increases. As explained from the simulations performed by Dong *et al.* [64], for a drop undergoing lateral vibrations on a vertical surface, gravity aids the inertial force on the drop during the downward lateral motion of the drop. For larger droplets, the net force due to gravity is larger as compared to smaller droplets. This results in smaller threshold accelerations for larger droplets as compared to smaller droplets.

Fig. 51 shows the sliding threshold acceleration at the resonance frequency as a function of static contact angle. For each droplet volume, as the static contact angle increases, the required sliding threshold acceleration reduces. For each droplet volume, PTFE requires the lowest amount of acceleration and thus amplitude and vibrational intensity. This is because for surfaces having smaller static contact angles, the center of gravity of the droplet is closer to the surface as compared to surfaces having a larger static contact angle, making the former droplets more stable on the low contact angle surface.
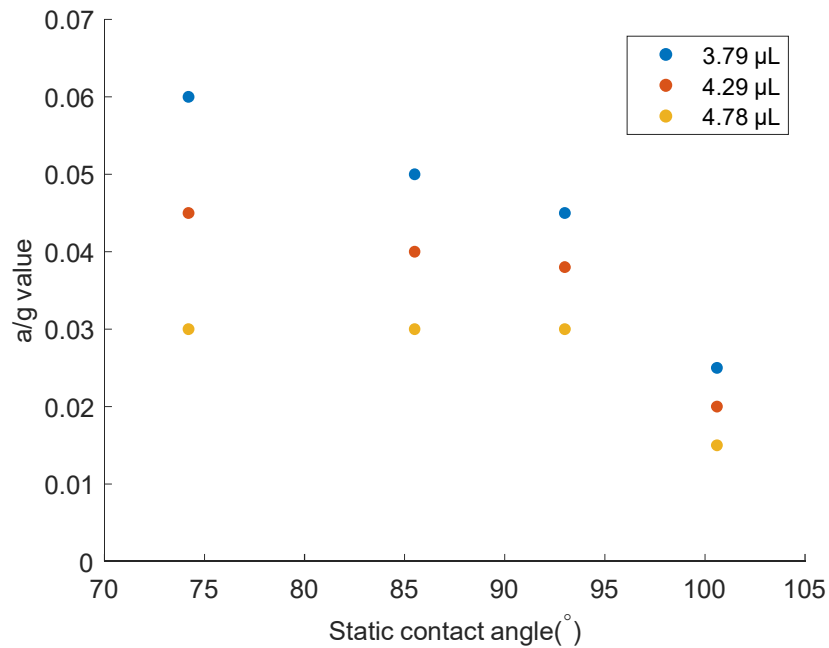
Figure 51. Droplet sliding threshold acceleration at resonance frequencies as a function of static contact angle

4.5 Dropwise condensation under lateral vibrations

4.5.1 Characterization of the substrate stand – cold plate – condensation surface

vibration system

As revealed from the literature, rocking mode resonance frequencies are the most effective in overcoming the contact angle hysteresis. Furthermore, in the previous two sections rocking mode resonance frequencies and their corresponding sliding threshold amplitudes were found. In the next stage of the study (i.e., dropwise condensation with vibrations), it is crucial to impose clean frequencies, which correspond to the rocking mode of the formed droplets. Thus, it is crucial to obtain clean frequencies corresponding to the rocking mode from the system without any interference from higher modes.

78

Therefore, initially, characterization of the frequency response of the substrate stand - cold plate – condensation surface system was conducted, to ensure that clean frequencies with no interference from higher order harmonics were obtained.

As described in Chapter 3, the cold plate – condensation surface assembly was firmly bolted to the substrate stand. The substrate stand was attached to the sound speaker, which provided the prescribed vibrations. The accelerometer was connected to the substrate stand to measure the frequency and acceleration of the stand. The vibration test was initiated by starting the chiller to have chilled water flowing through the cold plate. Then, different frequencies in the range of 50 - 75 Hz were provided to the speaker. The Fast Fourier Transform (FFT) of two of the frequencies tested for two different accelerations are shown in Figures 52 and 53.
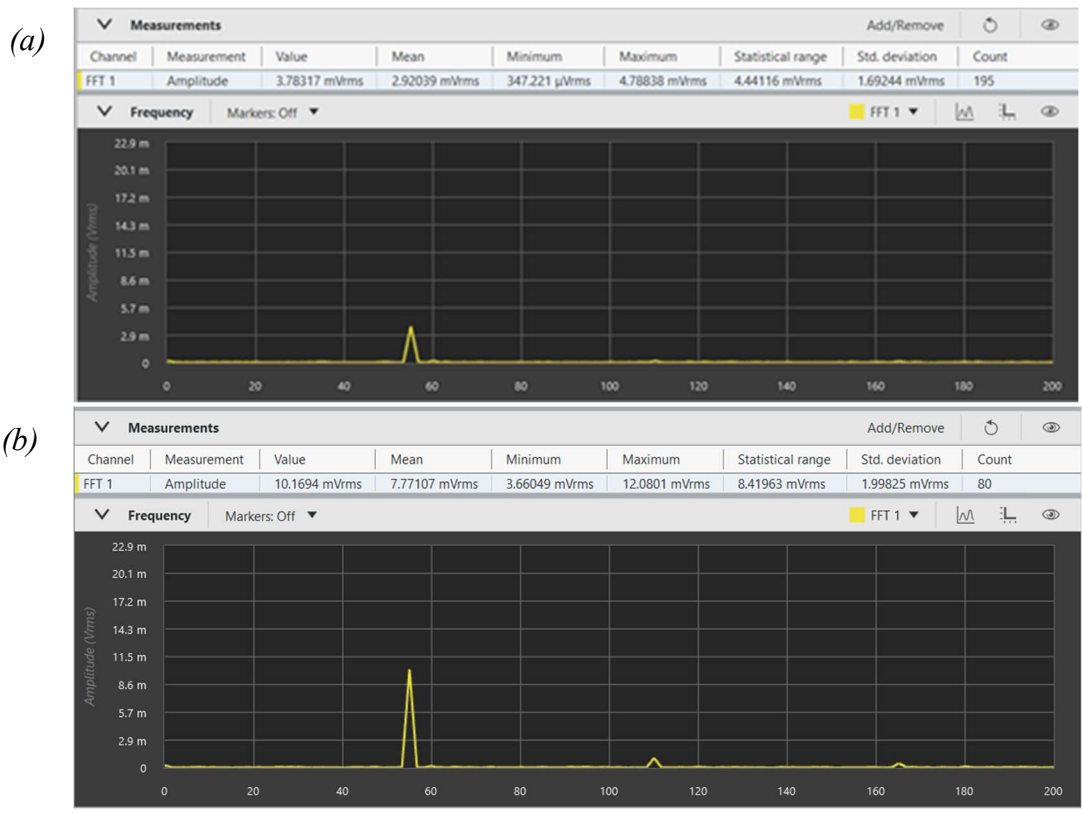
Figure 52. FFT for an imposed frequency on the whole system at 55Hz and at *(a)* 0.04g *(b)* 0.1g

(a)

(b)
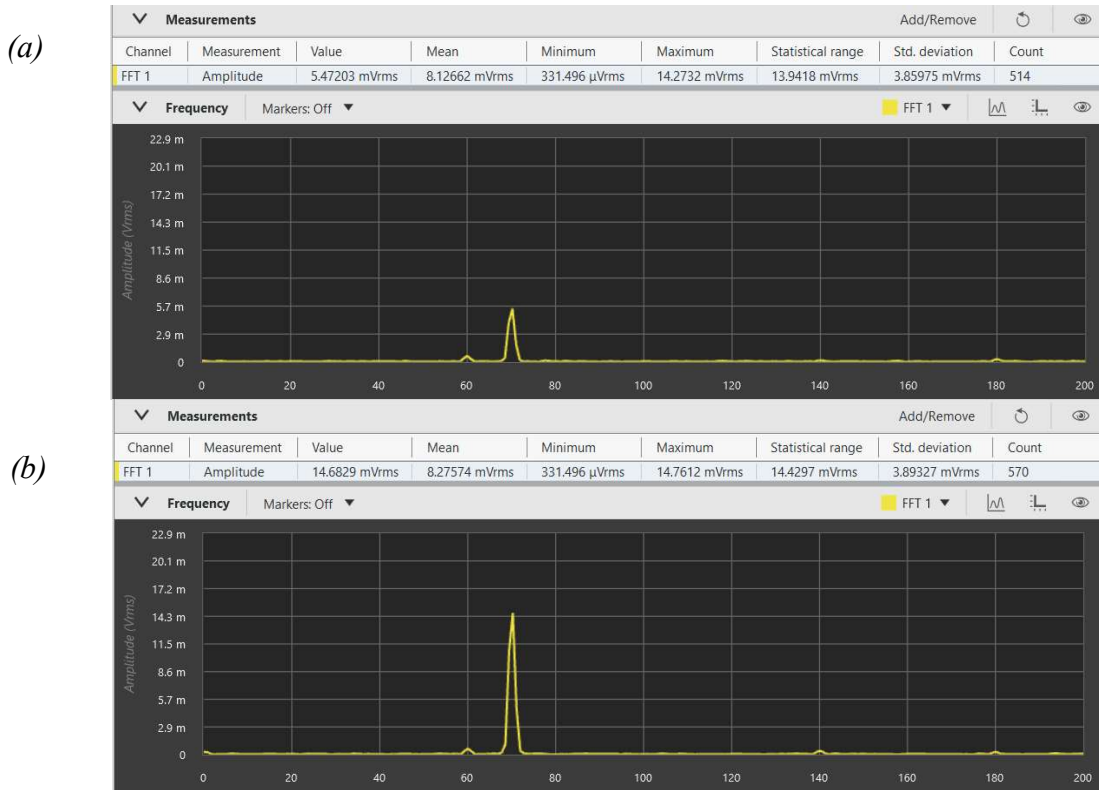
**Figure 53. FFT for an imposed frequency of the whole system at 70Hz and at *(a)*
0.055g *(b)* 0.14g**

As seen in Figures 52 and 53, clean frequencies with controlled amplitudes were
obtained from the system. In summary, the lab set up designed and built for the
condensation experiments behaved as expected and produced no higher-order harmonic
effects.

4.5.2 Effect of resonant vibrations on dropwise condensation for different surface types

Condensation experiments at constant sub-cooling were conducted using copper
110 and PTFE as substrates. The same copper surface used in the droplet wetting
experiments was also used in the condensation experiments. However, since the thermal

conductivity of PTFE is low, a 0.8 mm thick PTFE film was used. The sub-cooling value used ensured that there was pure dropwise condensation on each surface as shown in Fig. 54. For all the condensations tests, the last ten temperature data points were used to determine the average surface temperature and the moist air dry-bulb temperature values. All temperature values reported in the thesis were taken under steady-state conditions.
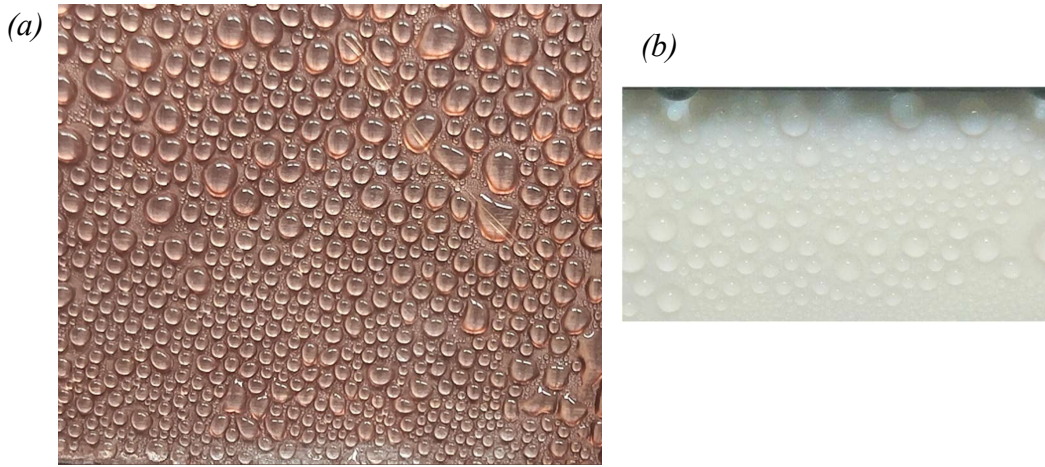
Figure 54. Dropwise condensation on *(a)* copper 110 *(b)* PTFE

The mass of the condensate for each test was collected and measured as described in Chapter 3. The heat transfer rate ($\dot{Q}_{latent}$), heat flux (Q''_{latent}) and heat transfer coefficient (h_{latent}) due to condensation were calculated from the mass of the condensate ($m_{condensate}$) by using Equations 23 through 25.

$$\dot{Q}_{latent} = \frac{m_{condensate} h_{fg}}{t} \qquad (23)$$

$$Q''_{latent} = \frac{\dot{Q}_{latent}}{SA} \qquad (24)$$

Where, $SA = L \cdot W$

$$h_{latent} = \frac{Q''_{latent}}{(T_{sat} - T_s)} \qquad (25)$$

where, SA, T_s and t are the surface area of the condensation surface, surface temperature

and time for condensate collection, respectively, while L and W are the length and width

of the surface. For the present study, both copper and PTFE surfaces used were 40 mm by

33 mm. h_{fg} is the latent heat of condensation for water at the bulk air temperature in the

chamber, T_b, which was obtained using Engineering Equation Solver (EES). T_{sat} (dew

point) was obtained using EES taking into account the dry bulb temperature measured in

the chamber (T_b) and relative humidity (%RH) measured inside the chamber.

To estimate the uncertainty in $\dot{Q}_{latent}$, Q''_{latent} and h_{latent}, Equations 26 through

28 were used

$$\Delta\dot{Q}_{latent} = \dot{Q}_{latent}\left(\frac{\Delta m_{condensate}}{m_{condensate}} + \frac{\Delta t}{t}\right) \qquad (26)$$

The condensate was measured using a micro-balance with an accuracy of $\pm$ 0.1mg. Thus,

the uncertainty in measurement of mass ($\Delta m_{condensate}$) is 0.1mg. The time was measured

using a stopwatch with a least count of $\Delta t = 1$ second.

$$\Delta Q''_{latent} = Q''_{latent}\left(\frac{\Delta\dot{Q}_{latent}}{\dot{Q}_{latent}} + \frac{\Delta A}{A}\right) \qquad (27)$$

Where, $\Delta A = L \cdot \Delta W + W \cdot \Delta L$

For the present study, both copper and PTFE surfaces used were 40 mm by 33 mm. A

vernier caliper with a least count of 0.1 mm was used to measure the dimensions of the

surface. Using the above equation, the uncertainty in area ΔA is calculated to be 7.3×10^{-6} m^2.

$$\Delta h_{latent} = h \left(\frac{\Delta Q''_{latent}}{Q''_{latent}} + \frac{\Delta(T_{sat} - T_s)}{(T_{sat} - T_s)} \right) \qquad (28)$$

Where, $\Delta(T_{sat} - T_s) = \Delta T_{sat} + \Delta T_s$

The uncertainty in ΔT_{sat} was calculated from EES to be equal to ± 1 $^\circ$C. It was obtained from the uncertainty in relative humidity measurement which was $\pm 3\%$ and the uncertainty in temperature measurement which was ± 0.5 $^\circ$C. Thus, the uncertainty in the level of sub-cooling was ± 1.5 $^\circ$C.

Figures 55 and 56 show the temperature – time graph for the moist air temperature and surface temperature for copper and PTFE, respectively. From the figures, it can be seen that steady state was reached after approximately one hour.
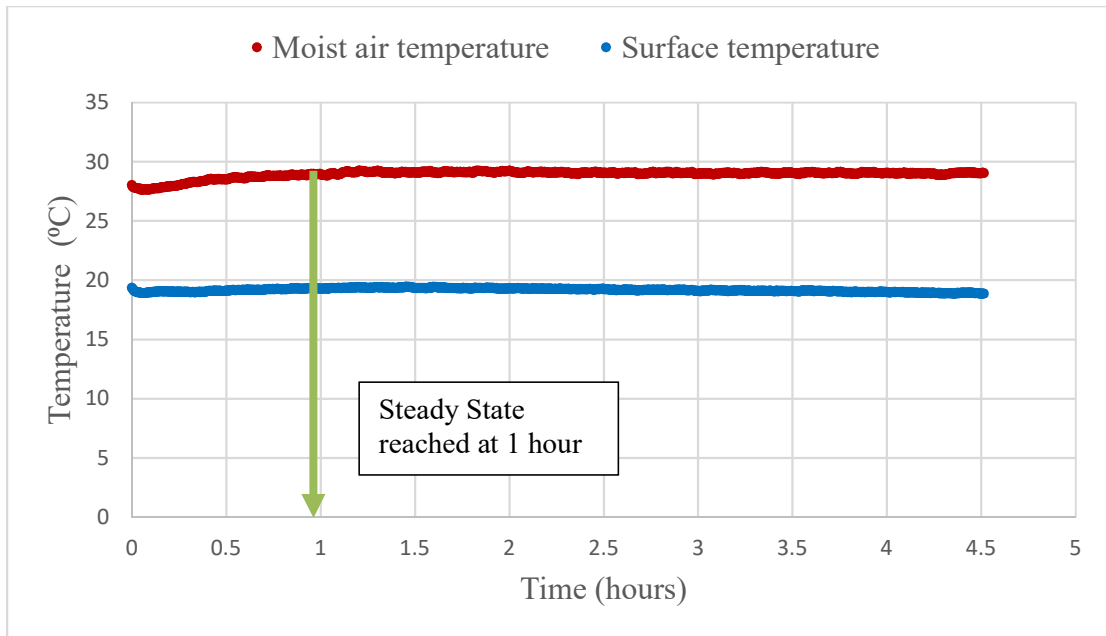
Figure 55. Moist air and surface temperature as a function time using copper 110 as substrate
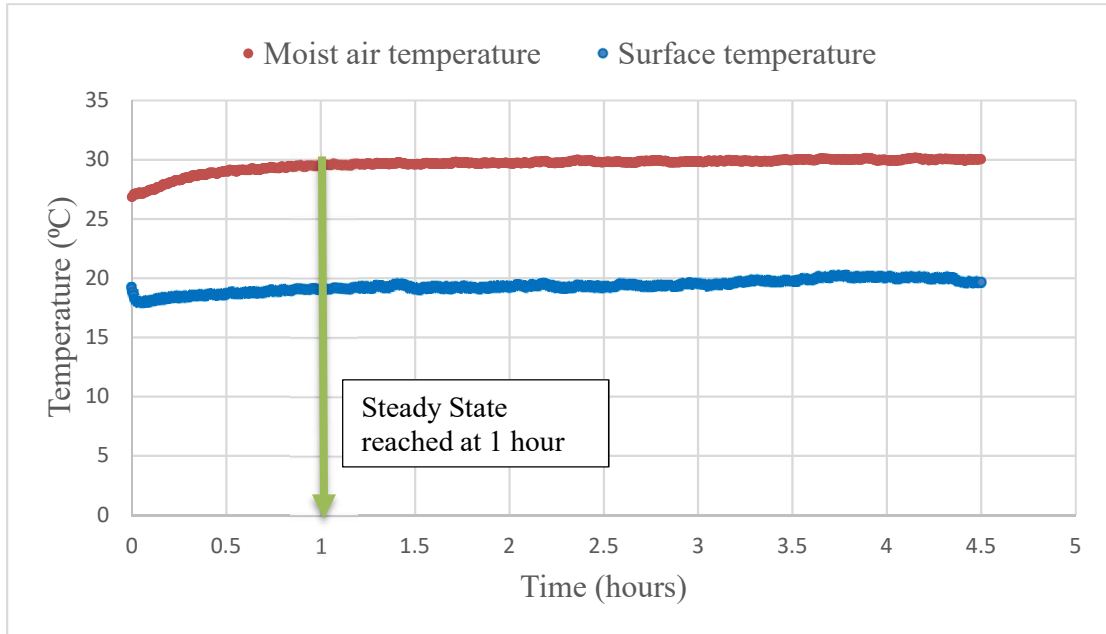
Figure 56. Moist air and surface temperature as a function time using PTFE as substrate

Table 9 provides dry bulb and saturation temperatures, and relative humidity under steady state conditions for the copper and PTFE condensation tests.

Table 9. Steady state conditions for dropwise condensation on copper 110 and PTFE

	Copper 110	PTFE
Dry Bulb Temperature (T_b) (°C)	29.1	29.8
Surface Temperature (T_s) (°C)	19.2	19.4
Relative Humidity (% RH)	96%	96%
Saturation Temperature (T_{sat}) (Dew point) (°C)	28.4	29.1
Sub-cooling $(T_{sat} - T_s)$ (°C)	9.2	9.7
Latent heat (h_{fg}), [J/g]	2432	2432

Table 10 and 11 show the results of the vibration tests on dropwise condensation, in which condensate mass was collected without vibration and with different vibration conditions using copper and PTFE as substrates. The imposed frequencies and amplitudes are shown in parentheses in the format $(f_{imposed}, a_{imposed})$. For the vibration tests in which the frequency varied with time (frequency sweeps), a single sweep started and finished at specific frequencies, while the imposed amplitudes were controlled in the range as shown in Table 10. Furthermore, the calculated values of heat transfer rate, heat flux and heat transfer coefficient are also shown in Table 10. The uncertainties of calculated values found using Equations 26 through 28 are given in the appendix.

Table 10. Condensation tests results with and without vibration using copper 110 as substrate

Vibration Condition (f, a)	Mass of Condensate[1] (grams)	% $m_{condensate}$ Enhancement	$\dot{Q}_{latent}$ (W)	Q''_{latent} $\left(\dfrac{W}{m^2}\right)$	h_{latent} $\left(\dfrac{W}{m^2 - {}^0C}\right)$
Without Vibration (0,0)	0.381	--	0.51	389.98	42.4
With Vibration (63, 0.06g)	0.425	11.5%	0.57	435.02	47.3
Frequency Sweep 50 – 70 Hz[2] (50 – 60, 0.045g – 0.06g) (61 – 70, 0.065g – 0.08g)	0.561	47.2%	0.76	574.22	62.4
Frequency Sweep 70 – 50 Hz[2] (70 – 61, 0.065g – 0.08g) (60 – 50, 0.045g – 0.06g)	0.712	86.9%	0.96	728.78	79.2
Note: (1) Mass of the condensate in each case is collected at equal time intervals of 30 minutes. (2) Each frequency sweep took 30 minutes or 1.5 minutes per frequency					

From Table 10, it can be seen that for copper, there is improvement in condensation in presence of vibrations. Imposing a single frequency of 63 Hz and single acceleration of 0.06g, led to a small improvement of ~12% in condensation rates as compared to the without-vibration case (base case). Imposing a frequency sweep from 50 – 70 Hz, led to a ~ 47% increase in condensation rates as compared to the base case. Furthermore, a frequency sweep from 70 - 50 Hz, led to an even greater improvement of ~ 87% as compared to the base case and ~ 27% as compared to the 50-70 Hz sweep.

Vibrations also led to enhanced condensation rates on PTFE as shown in Table 11. When a single frequency and acceleration of 60.5 Hz and 0.03g were imposed, a ~12% improvement in condensation rate was observed. Imposing a frequency sweep from 50 – 70 Hz, led to a ~15 % increase in condensation rate as compared to the base case. Furthermore, reversing the direction of the sweep to 70 – 50 Hz, led to ~ 30% improvement in condensation rate in comparison to the base case.

Table 11. Condensation tests results with and without vibration using PTFE as substrate

Vibration Condition (f, a)	Mass of Condensate [1](grams)	% $m_{condensate}$ Enhancement	$\dot{Q}_{latent}$ (W)	Q''_{latent} $\left(\dfrac{W}{m^2}\right)$	h_{latent} $\left(\dfrac{W}{m^2 - {}^0C}\right)$
Without Vibration (0,0)	0.265	--	0.36	271.25	28.0
With Vibration (60.5, 0.03g)	0.298	12.5%	0.40	305.02	31.5
Frequency Sweep 50 – 70 Hz[2] (50 – 60, 0.02g – 0.03g) (61 – 70, 0.03g – 0.04g)	0.305	15.1%	0.41	312.19	32.2
Frequency Sweep 70 – 50 Hz[2] (70 – 61, 0.03g – 0.04g) (60 – 50, 0.02g – 0.03g)	0.344	29.8%	0.46	352.11	36.3
Note: (1) Mass of the condensate in each case is collected at equal time intervals of 30 minutes (2) Each frequency sweep took 30 minutes or 1.5 minutes per frequency					

When imposing a single resonance frequency on both surfaces individually, it only excited a small fraction of droplet volumes that had similar resonance frequencies. This could be a reason for the small improvement in condensation rates, which was observed in both surfaces. Migliaccio [11] did a similar condensation experiment, where he imposed

four different single frequencies (i.e., 100Hz, 200Hz, 300Hz and 400Hz) on a hydrophobic surface and obtained a maximum improvement of 70% for the 100 Hz case. However, the accelerations imposed in that study were large (in the range of 3g - 8g).

For both surfaces, a frequency sweep from 50 – 70 Hz (1.25 minutes per frequency) led to improvement in condensation rates. As a result, a wider range of droplet volumes resonated and shed during the frequency sweep, which is probably the main reason for the observed improvement. This was also observed by Moradi *et al.* [15] in their study investigating the effects of longitudinal vibrations on dropwise condensation. For each surface, a frequency sweep from 70 – 50 Hz led to the greatest improvements in condensation rates as compared with all the other cases. This improvement can be potentially attributed to the direction of the sweep from high to low frequencies. For a 50 – 70 Hz sweep, larger droplets resonated and shed first, taking along smaller droplets with them during shedding events. On the other hand, for a 70 – 50 Hz sweep, smaller droplets resonated first, leading to improved droplet coalescence, and shedding of more droplets simultaneously. Therefore, the higher improvement in condensation rate seen in the 70 – 50 Hz sweep could be due to a higher number of smaller droplets resonating and shedding simultaneously at a given point, leading to greater rate of droplet coalescence.

However, the condensation rate enhancement when imposing 50 – 70 Hz sweeps were higher in the case of copper than in the case of PTFE. Furthermore, when the direction of the sweep was reversed to 70 – 50 Hz, a similar behavior was observed (i.e., a lower improvement for PTFE than copper). It is worth noting that the steady state conditions in both cases were similar as shown in Table 9.

89
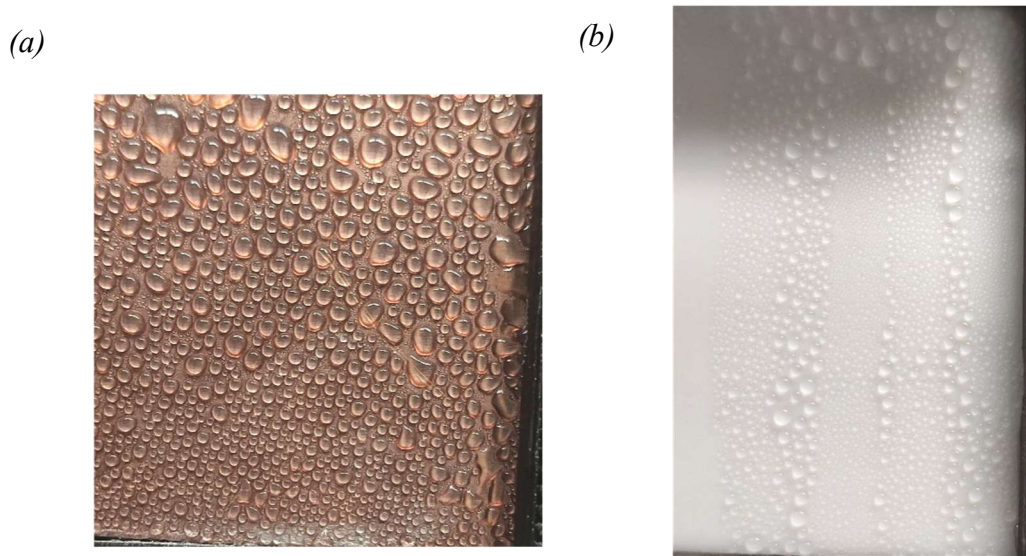
Figure 57. Snapshots of dropwise condensation on (a) copper (b) PTFE taken at the end of a frequency sweep

Fig. 57 shows dropwise condensation on both copper and PTFE surfaces right at the end of a frequency sweep. As the figure shows, PTFE contains smaller droplets than the copper surface even though adequate acceleration ratio (a/g) was imposed. A similar behavior was observed by Yao *et al.* [81] when they studied dropwise condensation on PTFE without the effects of vibration. Furthermore, the large percentage of smaller droplets seen on PTFE is due to the low surface roughness [75], which contributes to low contact angle hysteresis and smaller maximum radii of droplets as predicted by Equation 4 [9]. Moreover, since PTFE has low thermal conductivity, droplets take more time to grow on the surface as compared to copper. Also, smaller droplets require higher frequencies and greater accelerations to resonate and shed. Furthermore, even if smaller droplets shed, with or without external vibrations, they tend to sweep a smaller surface area of droplets as compared to larger droplets. Overall, these two factors could explain

for the low condensation enhancement rate enhancement rate for PTFE as compared to copper.

CHAPTER V

CONCLUSIONS AND FUTURE WORK

5.1 Conclusions

The main objective of this work was to study the effect of resonant vibrations on droplet mobility and dropwise condensation on vertically oriented solid surfaces. Five surfaces, namely, aluminum 6061, copper 110, polystyrene, PTFE and wax were used in this study. Initially, the static contact angle of 3 - 5 μL DI water droplets on all the substrates was determined.

In the next part of the study, resonance frequency was identified for four different droplet volumes ranging from 3 - 5 μL on all the surfaces, which were vertically oriented. For each droplet volume – surface combination, frequencies at which the droplets experienced maximum contact angle hysteresis were identified as resonance frequencies. It was observed that, for each surface, the resonance frequency decreases with increasing droplet volume. Furthermore, for each droplet volume, the resonance frequency decreases with increasing static contact angle. The identified resonance frequencies were then compared with similar numerical and experimental resonance frequency identification studies. It was found that the experimentally identified resonance frequencies agree with the model developed by Sakakeeny *et al.* [68]. Furthermore, the Celestini's model was found to underpredict the identified resonance frequencies up to a maximum of 21% with an average relative difference of 17.3%.

The effect of resonance frequencies and frequencies within ± 8 Hz of the resonance frequencies on droplet sliding was investigated for the droplet volume – surface

combinations. It was observed that for each surface, the threshold amplitudes required for droplet sliding reduced as the droplet volumes increased. Furthermore, for each droplet volume the threshold amplitudes necessary for droplet sliding decreased with increasing static contact angle of the droplet on the surface. Moreover, for all droplet volume – surface combinations, the least amount of acceleration, vibration amplitude and vibrational energy were required at the resonance frequency.

Lastly, an exploratory study on dropwise condensation on copper and PTFE in the presence of resonant vibrations was conducted. It was observed that by imposing a single frequency and amplitude led to a small improvement in condensate collected, close to ~12% for both surfaces. The frequency sweep from 70 – 50 Hz produced the most condensation enhancement for both surfaces. Furthermore, the enhancement in condensation rates produced in presence of vibrations was found to be low in the case of PTFE as compared to copper. This was explained based on the observation of large number of small droplets on PTFE as compared to copper.

In conclusion, imposing resonant frequencies were found to achieve droplet mobility on the surface with the least amount of vibrational energy. Imposing resonant vibrations (resonant frequencies and droplet sliding threshold accelerations) were found to improve dropwise condensation rates with copper outperforming PTFE as condensation surface in presence of resonant vibrations.

5.2 Future work

Based on this work, the following objectives should be considered in future studies:

1. Conduct experiments using different fluids with surface tension values to cover a larger range of Bo number and study their effects on the resonance frequency of droplets.

2. Develop an imaging system to study the effects of vibrations on drop size distribution during dropwise condensation.

3. Investigate dropwise condensation with and without vibrations on bio-inspired surfaces

4. Study the effects of resonant vibrations on the heat transfer performance in a shell and tube heat exchanger

REFERENCES

1. Incropera, F.P. and D.P. DeWitt, *Fundamentals of heat and mass transfer*. 5th ed. ed. 2002, New York: J. Wiley.

2. Al-Shammari, S.B., D.R. Webb, and P. Heggs, *Condensation of steam with and without the presence of non-condensable gases in a vertical tube.* Desalination, 2004. **169**(2): p. 151-160.

3. Fu, W., et al., *Numerical investigation of convective condensation with the presence of non-condensable gases in a vertical tube.* Nuclear Engineering and Design, 2016. **297**: p. 197-207.

4. Bum-Jin, C., et al., *Experimental comparison of film-wise and drop-wise condensations of steam on vertical flat plates with the presence of air.* International Communications in Heat and Mass Transfer, 2004. **31**(8): p. 1067-1074.

5. Rose, J.W., *Dropwise condensation theory and experiment: a review.* Proceedings of the Institution of Mechanical Engineers Part a-Journal of Power and Energy, 2002. **216**(A2): p. 115-128.

6. White, L.R., *On deviations from Young's equation.* Journal of the Chemical Society, Faraday Transactions 1: Physical Chemistry in Condensed Phases, 1977. **73**(0): p. 390-398.

7. Zhao, H., et al., *Scalable Slippery Omniphobic Covalently Attached Liquid Coatings for Flow Fouling Reduction.* ACS Appl Mater Interfaces, 2021. **13**(32): p. 38666-38679.

8. Lu, K.J., Y. Chen, and T.S. Chung, *Design of omniphobic interfaces for membrane distillation - A review.* Water Res, 2019. **162**: p. 64-77.

9. Kim, S. and K.J. Kim, *Dropwise Condensation Modeling Suitable for Superhydrophobic Surfaces.* Journal of Heat Transfer, 2011. **133**(8).

10. Zheng, S.F., U. Gross, and X.D. Wang, *Dropwise condensation: From fundamentals of wetting, nucleation, and droplet mobility to performance improvement by advanced functional surfaces.* Adv Colloid Interface Sci, 2021. **295**: p. 102503.

11.   Migliaccio, C.P., *Resonance-induced condensate shedding for high-efficiency heat transfer.* International Journal of Heat and Mass Transfer, 2014. **79**: p. 720-726.

12.   Laohalertdecha, S., P. Naphon, and S. Wongwises, *A review of electrohydrodynamic enhancement of heat transfer.* Renewable & Sustainable Energy Reviews, 2007. **11**(5): p. 858-876.

13.   Oh, I., et al., *Enhanced Condensation on Liquid-Infused Nanoporous Surfaces by Vibration-Assisted Droplet Sweeping.* ACS Nano, 2020. **14**(10): p. 13367-13379.

14.   Miljkovic, N., et al., *Jumping-droplet-enhanced condensation on scalable superhydrophobic nanostructured surfaces.* Nano Lett, 2013. **13**(1): p. 179-87.

15.   Moradi, M., S.F. Chini, and M.H. Rahimian, *Vibration-enhanced condensation heat transfer on superhydrophobic surfaces: An experimental study.* AIP Advances, 2020. **10**(9).

16.   Holden, K.M., et al., *The Use of Organic Coatings to Promote Dropwise Condensation of Steam.* Journal of Heat Transfer, 1987. **109**(3): p. 768-774.

17.   Ma, J., D.G. Cahill, and N. Miljkovic, *Condensation Induced Blistering as a Measurement Technique for the Adhesion Energy of Nanoscale Polymer Films.* Nano Lett, 2020. **20**(5): p. 3918-3924.

18.   Das, A.K., et al., *The Use of an Organic Self-Assembled Monolayer Coating to Promote Dropwise Condensation of Steam on Horizontal Tubes.* Journal of Heat Transfer, 2000. **122**(2): p. 278-286.

19.   Chen, L., et al., *n-Octadecanethiol self-assembled monolayer coating with microscopic roughness for dropwise condensation of steam.* 2009. **18**(2): p. 160-165.

20.   Vemuri, S., et al., *Long term testing for dropwise condensation using self-assembled monolayer coatings of n-octadecyl mercaptan.* Applied Thermal Engineering, 2006. **26**(4): p. 421-429.

21.   Guohua Yang, N.A.A., † Zane B. Starkewolfe,‡ and Gang-yu Liu*,†, *Molecular-Level Approach To Inhibit Degradations of Alkanethiol Self-Assembled Monolayers in Aqueous Media.* Langmuir, 2004. **20**: p. 3995-4003.

22.   Preston, D.J., et al., *Effect of hydrocarbon adsorption on the wettability of rare earth oxide ceramics.* Applied Physics Letters, 2014. **105**(1).

23.   Shim, J., et al., *Condensation Heat-Transfer Performance of Thermally Stable Superhydrophobic Cerium-Oxide Surfaces.* ACS Appl Mater Interfaces, 2018. **10**(37): p. 31765-31776.

24.   Preston, D.J., et al., *Scalable graphene coatings for enhanced condensation heat transfer.* Nano Lett, 2015. **15**(5): p. 2902-9.

25.   Bani Kananeh, A., et al., *Experimental study of dropwise condensation on plasma-ion implanted stainless steel tubes.* International Journal of Heat and Mass Transfer, 2006. **49**(25-26): p. 5018-5026.

26.   Leipertz, A. and A.P. Fröba, *Improvement of Condensation Heat Transfer by Surface Modifications.* Heat Transfer Engineering, 2010. **29**(4): p. 343-356.

27.   Woodruff, D.W. and J.W. Westwater, *Steam condensation on electroplated gold: Effect of plating thickness.* International Journal of Heat and Mass Transfer, 1979. **22**(4): p. 629-632.

28.   Schrader, M.E., *Ultrahigh-vacuum techniques in the measurement of contact angles. II. Water on gold.* The Journal of Physical Chemistry, 2002. **74**(11): p. 2313-2317.

29.   Enright, R., et al., *Dropwise Condensation on Micro- and Nanostructured Surfaces.* Nanoscale and Microscale Thermophysical Engineering, 2014. **18**(3): p. 223-250.

30.   Yao, C.-W., et al., *Wetting behavior on hybrid surfaces with hydrophobic and hydrophilic properties.* Applied Surface Science, 2014. **290**: p. 59-65.

31.   Alwazzan, M., et al., *Condensation on hybrid-patterned copper tubes (I): Characterization of condensation heat transfer.* International Journal of Heat and Mass Transfer, 2017. **112**: p. 991-1004.

32.   Yang, K.-S., et al., *Experimental investigation of moist air condensation on hydrophilic, hydrophobic, superhydrophilic, and hybrid hydrophobic-hydrophilic surfaces.* International Journal of Heat and Mass Transfer, 2017. **115**: p. 1032-1041.

33.   Cha, H., et al., *Dropwise condensation on solid hydrophilic surfaces.* Sci Adv, 2020. **6**(2): p. eaax0746.

34.   Enright, R., et al., *Condensation on superhydrophobic surfaces: the role of local energy barriers and structure length scale.* Langmuir, 2012. **28**(40): p. 14424-32.

35. Enright, R., et al., *How coalescing droplets jump.* ACS Nano, 2014. **8**(10): p. 10352-62.

36. Zhu, J., et al., *Clustered ribbed-nanoneedle structured copper surfaces with high-efficiency dropwise condensation heat transfer performance.* ACS Appl Mater Interfaces, 2015. **7**(20): p. 10660-5.

37. Wen, R., et al., *Wetting Transition of Condensed Droplets on Nanostructured Superhydrophobic Surfaces: Coordination of Surface Properties and Condensing Conditions.* ACS Appl Mater Interfaces, 2017. **9**(15): p. 13770-13777.

38. Wong, T.S., et al., *Bioinspired self-repairing slippery surfaces with pressure-stable omniphobicity.* Nature, 2011. **477**(7365): p. 443-7.

39. Xiao, R., et al., *Immersion condensation on oil-infused heterogeneous surfaces for enhanced heat transfer.* Sci Rep, 2013. **3**: p. 1988.

40. Preston, D.J., et al., *Heat Transfer Enhancement During Water and Hydrocarbon Condensation on Lubricant Infused Surfaces.* Sci Rep, 2018. **8**(1): p. 540.

41. Butrymowicz, D., J. Karwacki, and M. Trela, *Condensation enhancement by means of electrohydrodynamic techniques.* Archives of Thermodynamics, 2014. **35**(4): p. 3-27.

42. Velkoff, H.R. and J.H. Miller, *Condensation of Vapor on a Vertical Plate with a Transverse Electrostatic Field.* Journal of Heat Transfer, 1965. **87**(2): p. 197-&.

43. Choi, H.Y., *Electrohydrodynamic Condensation Heat Transfer.* Journal of Heat Transfer, 1968. **90**(1): p. 98-102.

44. Didkovsky, A.B. and M.K. Bologa, *Vapor Film Condensation Heat-Transfer and Hydrodynamics under the Influence of an Electric-Field.* International Journal of Heat and Mass Transfer, 1981. **24**(5): p. 811-819.

45. Bejan, A. and A.D. Kraus, *Heat transfer handbook.* 2003, J. Wiley: New York.

46. Mugele, F. and J.-C. Baret, *Electrowetting: from basics to applications.* Journal of Physics: Condensed Matter, 2005. **17**(28): p. R705-R774.

47. Dey, R., et al., *Controlling shedding characteristics of condensate drops using electrowetting.* Applied Physics Letters, 2018. **113**(24).

48.   Wikramanayake, E.D. and V. Bahadur, *Electrowetting-based enhancement of droplet growth dynamics and heat transfer during humid air condensation.* International Journal of Heat and Mass Transfer, 2019. **140**: p. 260-268.

49.   Gao, L. and T.J. McCarthy, *Contact angle hysteresis explained.* Langmuir, 2006. **22**(14): p. 6234-7.

50.   Rahimzadeh, A. and M. Eslamian, *Experimental study on the evaporation of sessile droplets excited by vertical and horizontal ultrasonic vibration.* International Journal of Heat and Mass Transfer, 2017. **114**: p. 786-795.

51.   Andrieu, C., C. Sykes, and F. Brochard, *Average Spreading Parameter on Heterogeneous Surfaces.* Langmuir, 1994. **10**(7): p. 2077-2080.

52.   Boreyko, J.B. and C.H. Chen, *Restoring superhydrophobicity of lotus leaves with vibration-induced dewetting.* Phys Rev Lett, 2009. **103**(17): p. 174502.

53.   Brunet, P., J. Eggers, and R.D. Deegan, *Vibration-Induced Climbing of Drops.* Physical Review Letters, 2007. **99**(14): p. 144501.

54.   Sartori, P., et al., *Drop motion induced by vertical vibrations.* 2015. **17**(11): p. 113017.

55.   Lamb, H., *Hydrodynamics*. 1932: Cambridge University Press, UK.

56.   Strani, M. and F. Sabetta, *Free vibrations of a drop in partial contact with a solid support.* Journal of Fluid Mechanics, 1984. **141**: p. 233-247.

57.   Quéré, D., M.-J. Azzopardi, and L. Delattre, *Drops at Rest on a Tilted Plane.* Langmuir, 1998. **14**(8): p. 2213-2216.

58.   Noblin, X., A. Buguin, and F. Brochard-Wyart, *Vibrated sessile drops: Transition between pinned and mobile contact line oscillations.* The European Physical Journal E, 2004. **14**(4): p. 395-404.

59.   Daniel, S., et al., *Ratcheting Motion of Liquid Drops on Gradient Surfaces.* Langmuir, 2004. **20**(10): p. 4085-4092.

60.   Mettu, S. and M.K. Chaudhury, *Motion of Drops on a Surface Induced by Thermal Gradient and Vibration.* 2008. **24**(19): p. 10833-10837.

61.   Celestini, F. and R. Kofman, *Vibration of submillimeter-size supported droplets.* Physical Review E, 2006. **73**(4): p. 041602.

62.   Daniel, S., M.K. Chaudhury, and P.G. De Gennes, *Vibration-Actuated Drop Motion on Surfaces for Batch Microfluidic Processes.* Langmuir, 2005. **21**(9): p. 4240-4248.

63.   Sharp, J.S., D.J. Farmer, and J. Kelly, *Contact angle dependence of the resonant frequency of sessile water droplets.* Langmuir, 2011. **27**(15): p. 9367-71.

64.   Dong, L., A. Chaudhury, and M.K. Chaudhury, *Lateral vibration of a water drop and its motion on a vibrating surface.* The European Physical Journal E, 2006. **21**(3): p. 231-242.

65.   Yao, C.-W., et al., *Experimental study on effect of surface vibration on micro textured surfaces with hydrophobic and hydrophilic materials.* Applied Surface Science, 2017. **412**: p. 45-51.

66.   Huber, R.A., et al., *Vibration-Enhanced Droplet Motion Modes: Simulations of Rocking, Ratcheting, Ratcheting With Breakup, and Ejection.* Journal of Fluids Engineering, 2019. **141**(7): p. 071105.

67.   Sakakeeny, J. and Y. Ling, *Numerical study of natural oscillations of supported drops with free and pinned contact lines.* Physics of Fluids, 2021. **33**(6).

68.   Sakakeeny, J., et al., *A model to predict the oscillation frequency for drops pinned on a vertical planar surface.* Journal of Fluid Mechanics, 2021. **928**.

69.   *Investigation of the use of acoustic vibrations to improve heat transfer rates and reduce scaling in distillation units used for Saline water conversion.* Research and development progress report / United States Dept. of the Interior ;no. 65. 1962, Washington. D.C: U.S. Dept. of Commerce : For sale by the U.S. Dept. of Commerce, Office of Technical Services. xv, 141 p.

70.   Dent, J.C., *Effect of Vibration on Condensation Heat Transfer to a Horizontal Tube.* Proceedings of the Institution of Mechanical Engineers, 1969. **184**(1): p. 99-106.

71.   Dent, J., *The calculation of heat transfer coefficient for condensation of steam on a vibrating vertical tube.* International Journal of Heat and Mass Transfer, 1969. **12**(9): p. 991-996.

72.   Zhang, L., et al., *Experimental Study on Distribution Characteristics of Condensate Droplets Under Ultrasonic Vibration.* Microgravity Science and Technology, 2018. **30**(6): p. 737-746.

73.   Tong, W.L., et al., *Coupled effects of hydrophobic layer and vibration on thermal efficiency of two-phase closed thermosyphons.* RSC Advances, 2015. **5**(14): p. 10332-10340.

74.   Huber, R.A. and M.M. Derby. *Droplet Coalescence and Departure on a Vibrating Film During Humid Air Condensation*. in *ASME 2017 15th International Conference on Nanochannels, Microchannels, and Minichannels*. 2017.

75.   Deb, S.B., *Effects of Resonant Vibrations on Droplets for Enhanced Dropwise Condensation*. 2019, Texas A&M University.

76.   *Online Tone Generator*. Available from: http://onlinetonegenerator.com/.

77.   Rachmawan. *Canny Edge Detection (https://www.mathworks.com/matlabcentral/fileexchange/46859-canny-edge-detection)*. MATLAB Central File Exchange 2021 Retrieved September 27, 2021.

78.   Canny, J., *A computational approach to edge detection.* IEEE Trans Pattern Anal Mach Intell, 1986. **8**(6): p. 679-98.

79.   Rasband, W.S., *ImageJ*. 1997-2018: U. S. National Institutes of Health, Bethesda, Maryland, USA. p. https://imagej.nih.gov/ij/.

80.   Bostwick, J.B. and P.H. Steen, *Dynamics of sessile drops. Part 1. Inviscid theory.* Journal of Fluid Mechanics, 2014. **760**: p. 5-38.

81.   Yao, C.-W., *STUDY OF THE EFFECTS OF SURFACE MORPHOLOGY AND DROPLET GROWTH DYNAMICS ON CONDENSATION HEAT TRANSFER*, in *Mechanical Engineering*. 2014, Texas A&M University.
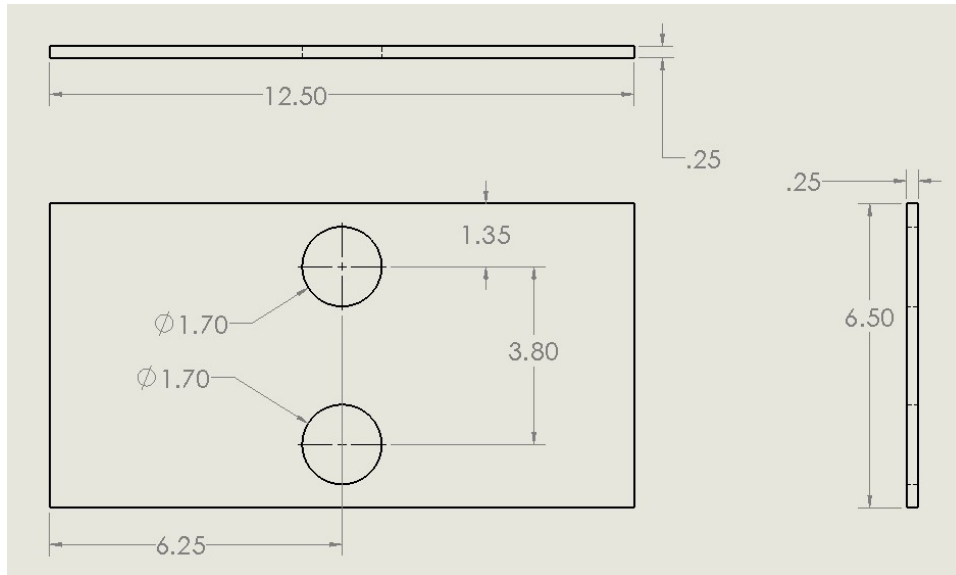
A.1 Outer chamber drawings

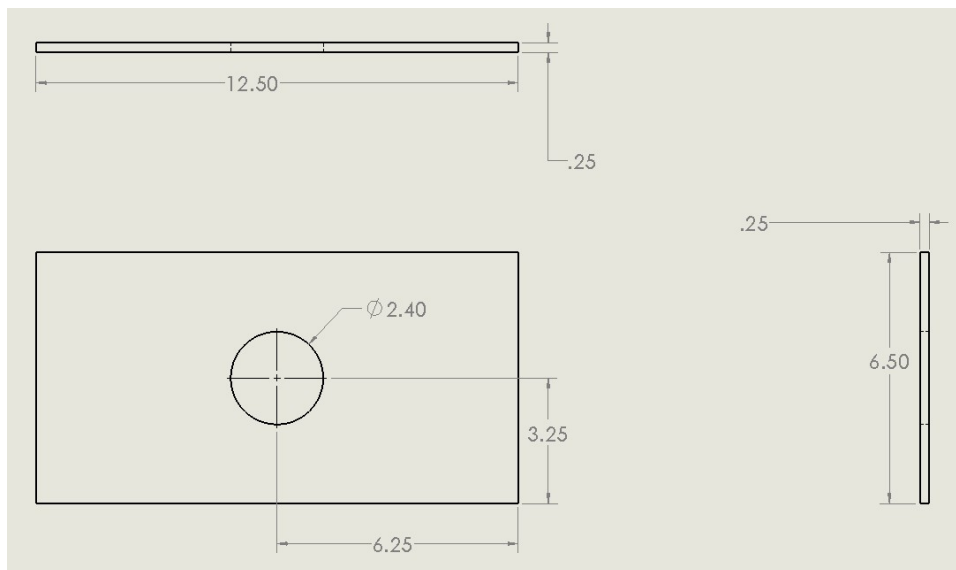All dimensions are in inches

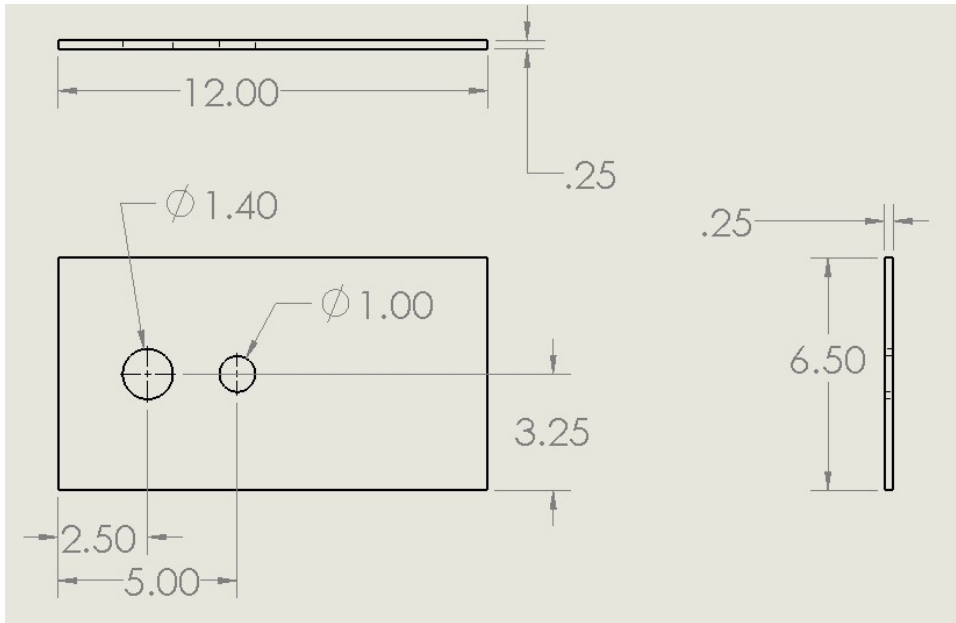**Figure A1. Outer chamber back wall**

Figure A2. Outer chamber front wall

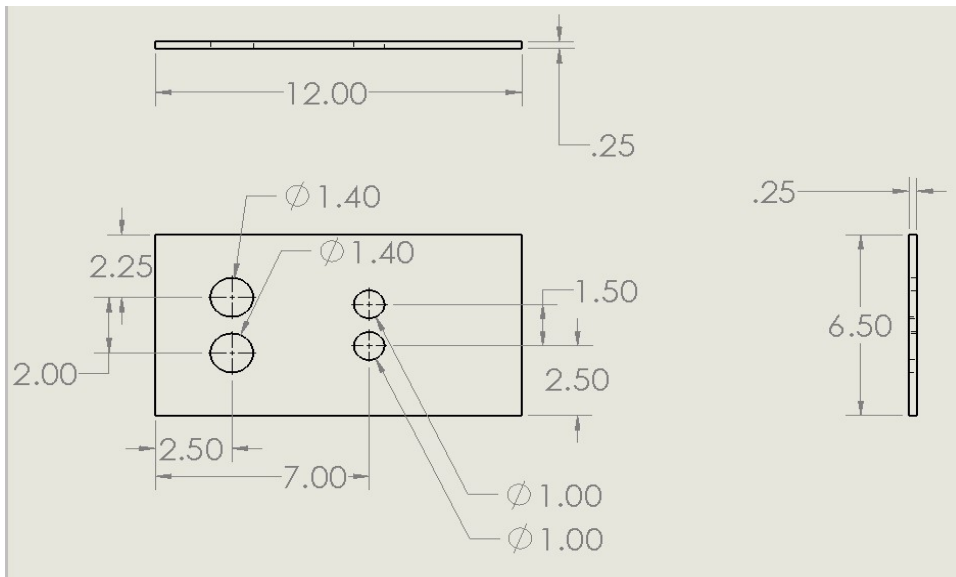**Figure A3. Outer chamber inlet wall**

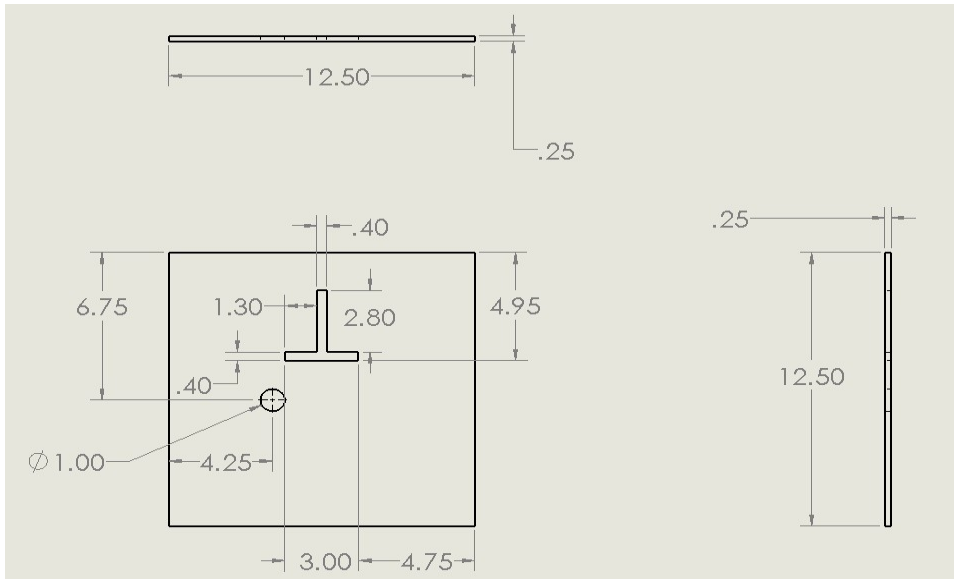**Figure A4. Outer chamber outlet wall**

103

Figure A5. Outer chamber top wall

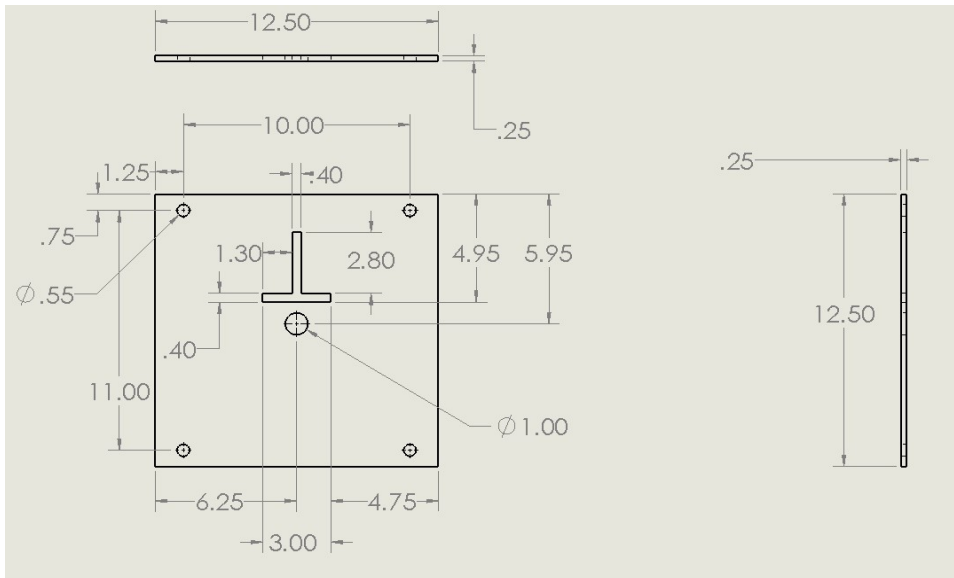**Figure A6. Outer chamber bottom wall**

A.2 Inner chamber drawings

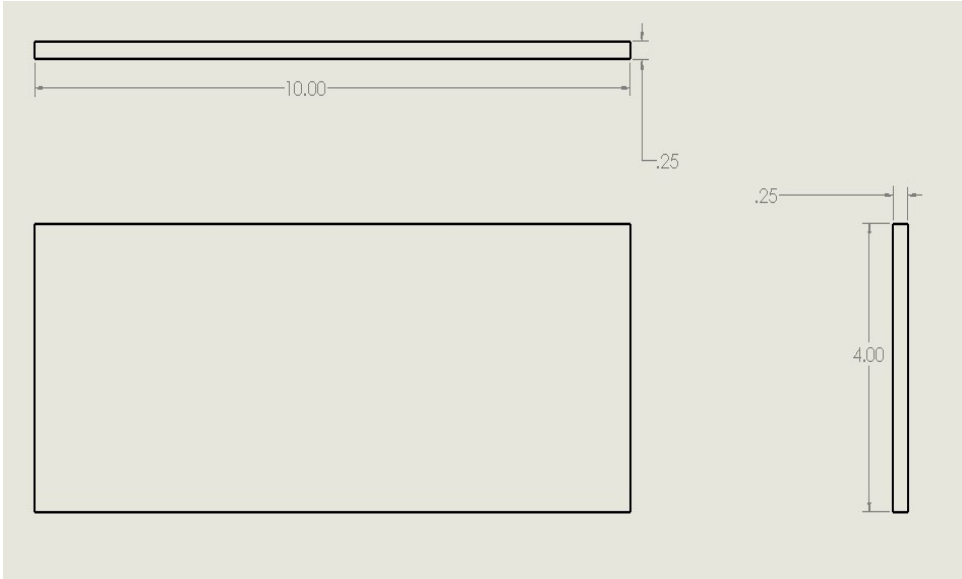All dimensions are in inches

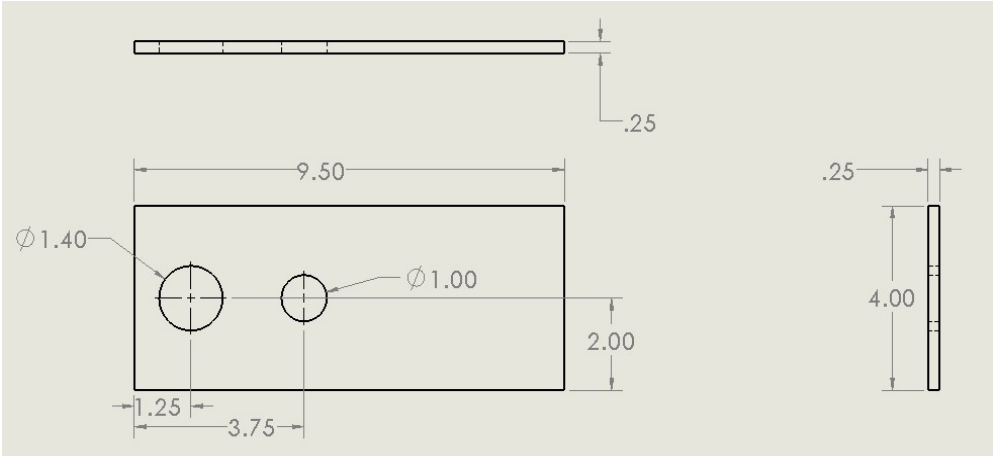**Figure A7. Inner chamber front and back walls**

Figure A8. Inner chamber inlet wall
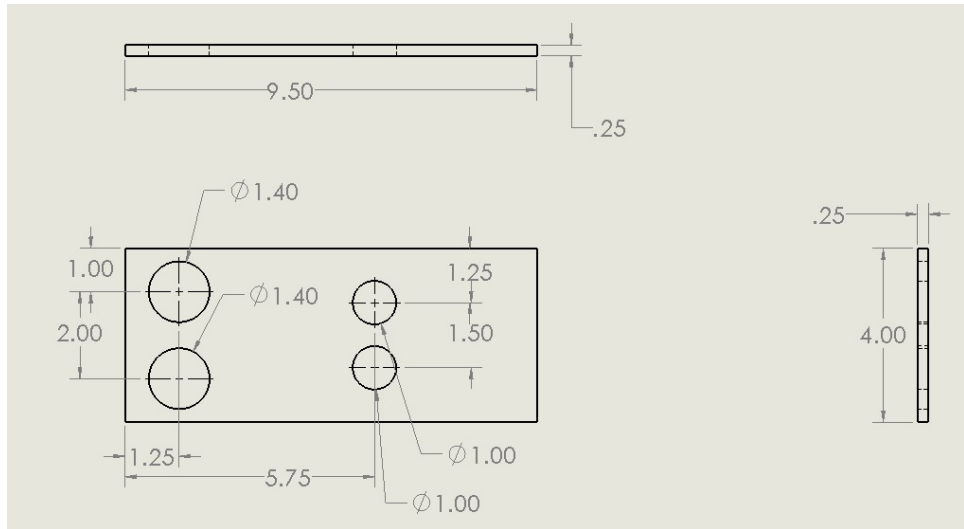
Figure A9. Inner chamber outlet wall
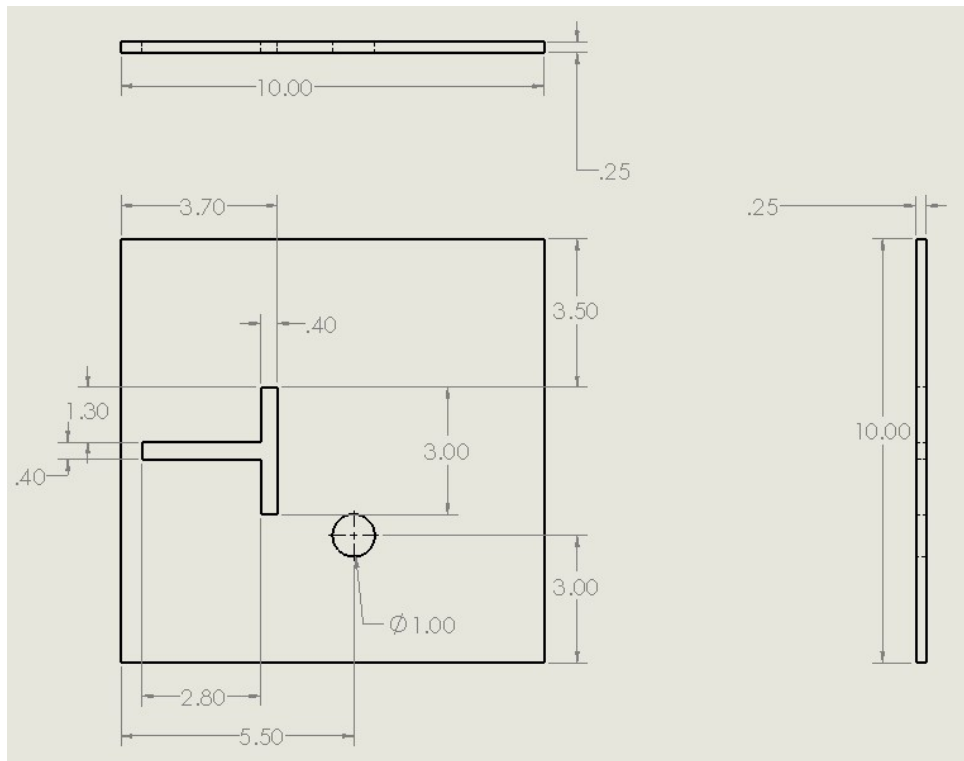
Figure A10. Inner chamber top wall
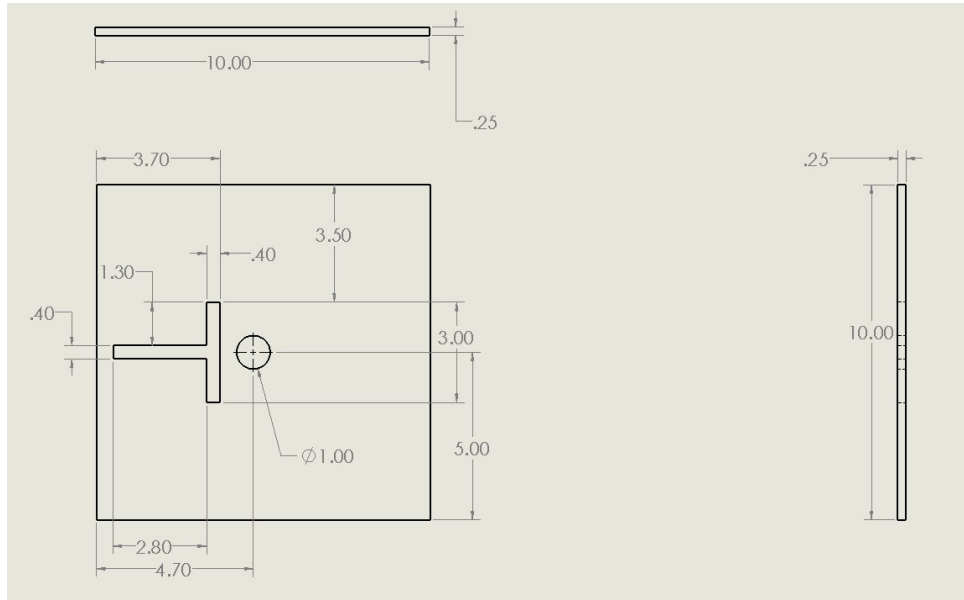
Figure A11. Inner chamber bottom wall

A.3 Substrate stand for condensation setup drawings

All dimensions are in inches

(a)   (b)

Figure A12. (a) Front part of the stand (b) Back support for the stand

A.4 Specifications for sound speaker Reference subwoofer 1070, Infinity Inc.

Figure A13. Dimensions for Reference subwoofer 1070, Infinity Inc.

Table A1. Specifications of sound speaker, Reference 1070, Infinity Inc.
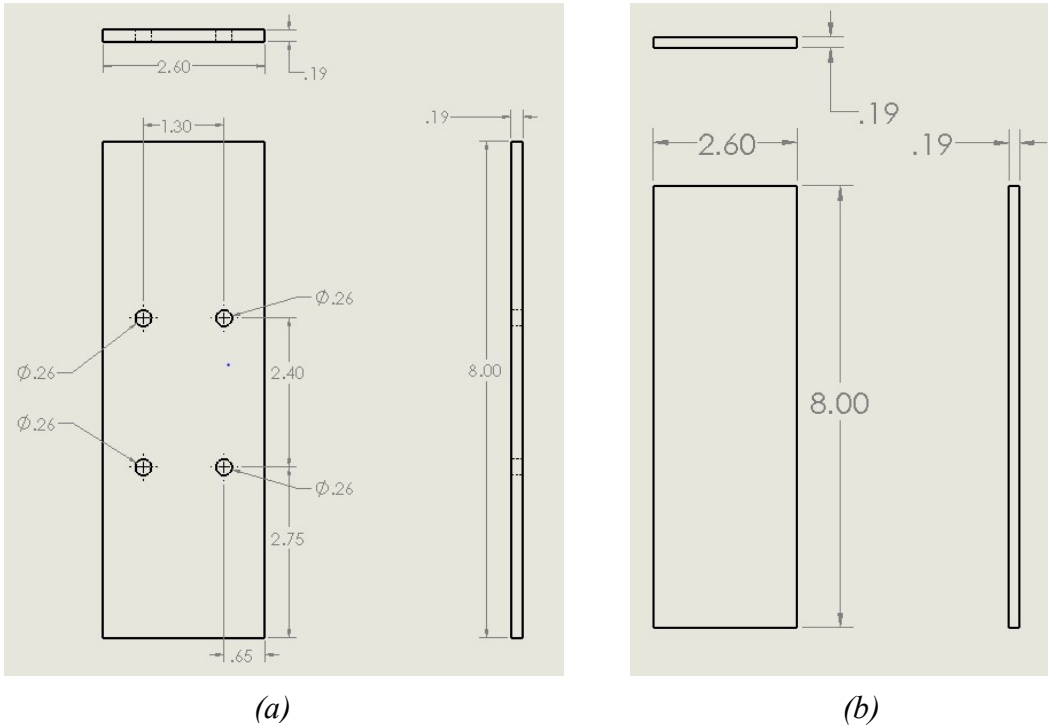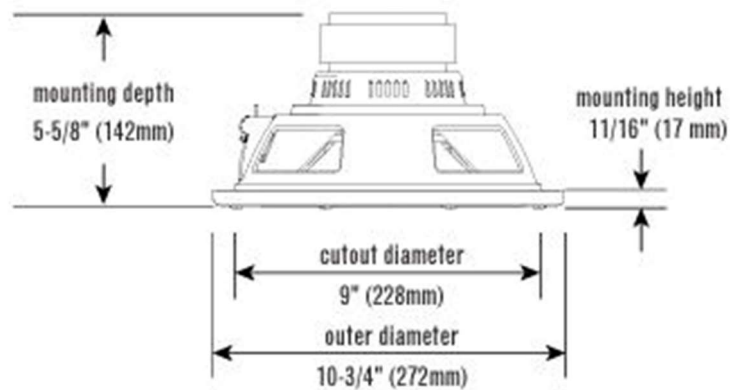
Woofer Diameter	10" (250 mm)
Power Handling	250W RMS, 1000W peak
Sensitivity (@ 2.83V)	93dB
Frequency Response	30Hz – 175Hz
Impedance	2 or 4 ohms, switch-selectable
Cutout Diameter	9" (228 mm)

A.5 Uncertainty analysis for resonance frequency identification

Table A2. Uncertainty analysis for normalized resonance frequencies

Static Contact Angle (SCA) (⁰)	Standard Deviation in SCA (⁰)	$f_{normalized}$ (-)	$f_{normalized}$ Upper Error Bar (-)	$f_{normalized}$ Lower Error Bar (-)
74.2	1.8	2.73	0.097	0.094
		2.68	0.099	0.088
		2.62	0.092	0.091
		2.65	0.072	0.112
85.5	1.3	2.16	0.042	0.041
		2.1	0.039	0.041
		2.05	0.045	0.034
		2.06	0.037	0.042
93	1.06	1.91	0.026	0.023
		1.85	0.027	0.021
		1.86	0.023	0.025
		1.86	0.025	0.023
100.6	0.7	1.682	0.011	0.012
		1.677	0.012	0.011
		1.681	0.012	0.011
		1.681	0.012	0.011
105	0.6	1.54	0.009	0.007
		1.52	0.006	0.01
		1.56	0.006	0.01
		1.56	0.003	0.013

A.6 Uncertainty analysis for condensation experiments

Table A3. Experimental cases

Case	Copper 110	PTFE
1	No vibration	No vibration
2	With Vibration (63Hz, 0.06g)	With Vibration (60.5Hz, 0.03g)
3	Frequency Sweep 50 – 70 Hz (50 – 60, 0.045g – 0.06g) (61 – 70, 0.065g – 0.08g)	Frequency Sweep 50 – 70 Hz (50 – 60, 0.015g – 0.03g) (61 – 70, 0.03g – 0.045g)
4	Frequency Sweep 70 – 50 Hz (61 – 70, 0.065g – 0.08g) (50 – 60, 0.045g – 0.06g)	Frequency Sweep 70 – 50 Hz (61 – 70, 0.03g – 0.045g) (50 – 60, 0.015g – 0.03g)

Table A4. Uncertainty analysis for heat transfer rate for copper 110 and PTFE

Case	Copper			PTFE		
	$\dot{Q}_{latent}$ (W)	$\Delta\dot{Q}_{latent}$ (W)	Uncertainty (%)	$\dot{Q}_{latent}$ (W)	$\Delta\dot{Q}_{latent}$ (W)	Uncertainty (%)
1	0.51	4.21×10^{-4}	0.082%	0.36	3.34×10^{-4}	0.093%
2	0.57	4.54×10^{-4}	0.080%	0.40	3.59×10^{-4}	0.089%
3	0.76	5.56×10^{-4}	0.073%	0.41	3.64×10^{-4}	0.088%
4	0.96	6.70×10^{-4}	0.070%	0.46	3.93×10^{-4}	0.085%

Table A5. Uncertainty analysis for heat flux rate for copper 110 and PTFE

	Copper			PTFE		
Case	Q''_{latent} $\left(\dfrac{W}{m^2}\right)$	$\Delta Q''_{latent}$ $\left(\dfrac{W}{m^2}\right)$	Uncertainty (%)	Q''_{latent} $\left(\dfrac{W}{m^2}\right)$	$\Delta Q''_{latent}$ $\left(\dfrac{W}{m^2}\right)$	Uncertainty (%)
1	367.70	2.27	0.62%	271.25	1.75	0.65%
2	410.16	2.52	0.61%	305.02	1.96	0.64%
3	541.41	3.30	0.61%	312.19	2.00	0.64%
4	687.14	4.16	0.61%	352.11	2.25	0.64%

Table A6. Uncertainty analysis for heat transfer coefficient for copper 110 and PTFE

	Copper			PTFE		
Case	h_{latent} $\left(\dfrac{W}{m^{2\,0}C}\right)$	Δh_{latent} $\left(\dfrac{W}{m^{2\,0}C}\right)$	Uncertainty (%)	h_{latent} $\left(\dfrac{W}{m^{2\,0}C}\right)$	Δh_{latent} $\left(\dfrac{W}{m^{2\,0}C}\right)$	Uncertainty (%)
1	39.97	6.76	17.2%	27.96	4.50	16.1%
2	44.58	7.54	16.9%	31.45	5.06	16.1%
3	58.85	9.95	16.9%	32.18	5.18	16.1%
4	74.69	12.63	16.9%	36.30	5.84	16.1%